Supporting Information

Advanced charge transfer technology for highly efficient and long-lived TADF-type organic afterglow with near infrared light excitable property

Guangming Wang,[#] Xuefeng Chen, [#] Jiahui Liu, Shuhui Ding and Kaka Zhang*

Key Laboratory of Synthetic and Self-Assembly Chemistry for Organic Functional Molecules, Shanghai Institute of Organic Chemistry, University of Chinese Academy of Sciences, Chinese Academy of Sciences, 345 Lingling Road, Shanghai 200032, People's Republic of China.

**Email: zhangkaka@sioc.ac.cn; #equal contribution.*

Table of Contents

triplet energy gap and relatively large SOCME of 0.68 cm^{-1} and 0.80 cm^{-1} when compared to S_1-to-T_1 ISC channel; S_1-to-T_2 and S_1-to-T_3 ISC channels facilitate the intersystem crossing of compound **1**. This is our understanding on the singlet-to-triplet ISC in compound **1** system. With the assist of PhB matrices, the **1**-PhB-0.01% materials exhibited RTP mechanim with long emission lifetimes (other afterglow mechanisms have been ruled out in Text S2).

Figure S4. The TD-DFT calculated results of compound 2 singlet and triplet excited states. From the results of TD-DFT calculation, it is found that S_1 and T_1 states of compound **2** showed similar excited state symmetry, while T_2 states exhibited different excited state nature from S_1 states. According to the El-Sayed rule, such different symmetry between S_1 and T_2 states would enhance singlet-to-triplet intersystem crossing. The S_1-to-T_2 ISC channel showed relatively small singlet-triplet energy gap and relatively large SOCME of 1.79 cm^{-1} when compared to S_1-to-T_1 ISC channel; S_1-to-T_2 ISC channel facilitates the intersystem crossing of compound **2**. This is our understanding on the singlet-to-triplet ISC in compound **2** system. With the assist of PhB matrices, the **2**-PhB-0.01% materials exhibited RTP mechanim with long emission lifetimes (other afterglow mechanisms have been ruled out in Text S2).

Figure S5. The TD-DFT calculated results of compound 3 singlet and triplet excited states. The TD-DFT calculated results of compound **3** singlet and triplet excited states. From the results of TD-DFT calculation, it is found S_1-to-T_1, S_1-to-T_2 and S_1-to-T_3 ISC channels possess relatively large SOCME of 0.46 cm^{-1}, 1.26 cm^{-1} and 0.54 cm^{-1}; these ISC channels facilitate the intersystem crossing of compound **3**. With the assist of PhB matrices, the **3**-PhB-0.01% materials exhibited RTP mechanim with long emission lifetimes (other afterglow mechanisms have been ruled out in Text S2).

Figure S6. The TD-DFT calculated results of compound 4 singlet and triplet excited states. From the results of TD-DFT calculation, it is found S_1-to-T_1, S_1-to-T_2 and S_1-to-T_3 ISC channels possess relatively large SOCME of 0.42 cm^{-1}, 0.43 cm^{-1} and 0.91 cm^{-1}; these ISC channels facilitate the intersystem crossing of compound **4**. With the assist of PhB matrices, the **4**-PhB-0.01% materials exhibited RTP mechanim with long emission lifetimes (other afterglow mechanisms have been ruled out in Text S2).

Figure S7. Room-temperature steady-state emission spectra of BF_2bdk in different solvents. DCM, EA, THF and ACE refer to dichloromethane, ethyl acetate, tetrahydrofuran and acetone, respectively.

Figure S8. (a) Schematic illustration of triplet-to-singlet excited state energy (TSET) from matrices to dopants in the reported studies. (b) Schematic illustration of the excited state energy levels in the present study. Significant afterglow properties in these systems can only be observed when the donors were sufficiently excited. The **5**-PhB-0.01% melt-cast material showed long-lived afterglow upon 365 nm or 405 nm excitation while PhB has negligible UV-vis absorption at 365 nm or 405 nm, so we reason that TSET is not responsible for the significant afterglow in the present system.

Figure S9. (a) Delayed emission (1 ms delay) spectra of **5**-PhB-0.01% melt-cast materials under ambient conditions. (b) Delayed emission (1 ms delay) of **5**-PhB-0.01% melt-cast materials under ambient conditions at 323 K.

Figure S10. UV-vis spectra of PhB. TD-DFT calculations (B3LYP functional and 6-31g (D, P) basis sets) were used to estimate the HOMO (-6.96 eV), LUMO (-1.79 eV), S_1 (4.52 eV) and T_1 (3.53 eV) levels of PhB.

Figure S11. (a) Schematic illustration of HOMO and LUMO levels of donors and acceptors with the involvement of intermolecular charge transfer. (b) Schematic illustration of HOMO and LUMO levels of compound **5** and PhB in the present study. PhB matrices possess higher-lying LUMO and lower-lying HOMO compared to **5**. The insignificant intermolecular charge transfer in **5**-matrix materials can rule out the contribution of donor-acceptor mechanism to the present organic afterglow system.

Figure S12. (a) Schematic illustration of the impurity mechanism for organic afterglow. (b) Schematic illustration of the separation of BF_2bdk and possible impurity by PhB matrices in the present study. In the present study, the high purity of **5** confirmed by HPLC measurement, as well as the similar maxima in UV-vis spectra and excitation spectra of **5**-PhB-0.01% melt-cast materials, can rule out the contribution of impurity mechanism to the present afterglow material systems.

Figure S13. (a) HPLC spectrum of compound **5**. UV absorption was monitored at 388 nm. (b) UV-vis spectra of compound **5** in different solvents. DCM, EA and THF refer

to dichloromethane, ethyl acetate and tetrahydrofuran, respectively. (c) Excitation spectra of **5**-PhB-0.01% samples.

Figure S14. Power-dependent delayed fluorescence spectra of **5**-PhB-0.01% samples. It is found that the intensity of delayed fluorescence of the afterglow materials exhibit a quasi-linear dependence on the excitation dose, which further support the TADF mechanism.

Figure S15. Chemdraw structure (left) and single crystal structure (right) of compound **5.**

Figure S16. Dependence of excited state properties on the conformation of BF_2bdk; here the conformation is defined by the dihedral angle between the second anisole group and the dioxaborine plane.

Figure S17. (a) HPLC spectrum of compound **6**. UV absorption was monitored at 382 nm. (b) UV-vis spectra of compound **6** in different solvents. DCM, EA and THF refer to dichloromethane, ethyl acetate and tetrahydrofuran, respectively. (c) Excitation spectra of **6**-PhB-0.01% samples.

Figure S18. Power-dependent delayed fluorescence spectra of **6**-PhB-0.01% samples. It is found that the intensity of delayed fluorescence of the afterglow materials exhibit a quasi-linear dependence on the excitation dose, which further support the TADF mechanism.

Figure S19. The TD-DFT calculated results of compound **6** singlet and triplet excited states. Despite that the singlet-triplet splitting energies ($\triangle E_{ST}$ = 0.43 eV) of **6**-PhB-0.01% system obtained from experimental results (S_1 level, 2.67 eV; T_1 level, 2.23 eV) are larger than those in **6**-PhB-0.01% system ($\triangle E_{ST}$ = 0.35 eV), there are rich S_1-to-T_n channels with SOCME values above 0.5 cm^{-1} and even 1.0 cm^{-1}. These would also enhance k_{RISC} of the **6**-PhB-0.01% to moderate values on the order of 10^0-10^1 s^{-1}, which agree well with the experimental observation (that is, the delayed fluorescence lifetimes 0.1 s to 1.0 s) of the **6**-PhB-0.01% materials under ambient conditions.

Figure S20. (a) Excited state decay profiles of **6**-PhB-0.01% melt-cast samples under ambient conditions. (b) The fluorescence decay profiles of **6**-PhB-0.01% melt-cast samples under ambient conditions.

Figure S21. Afterglow quantum yields (Φ_{AG}) and afterglow emission lifetimes (τ_{AG}) of organic RTP and afterglow materials in the previously reported studies.

Figure S22. (a) Room-temperature steady-state emission spectra of **6**-PhB-0.01% melt-cast materials (black line, in degassed condition; red line, in aerated condition). (b) Delayed emission spectra of **6**-PhB-0.01% melt-cast materials (black line, in degassed condition; red line, in aerated condition). (c) Room-temperature steady-state emission spectra of compound **6** in dichloromethane. (black line, in degassed condition; red line, in aerated condition).

Figure S23. Emission spectra of blue up-conversion materials (excited at 980 nm) from the supplier. The blue up-conversion materials were purchased from Shenzhen Orient Color Change Technology Co Ltd. The blue up-conversion materials are crystalline powders with sizes of around 5 μm.

Figure S24. Delayed emission (1 ms delay) spectra of 5-PhB-0.01% materials excited at 365 nm and 350 nm.

Figure S25. ^{1}H NMR spectra of compound **1**.

Figure S26. ^{1}H NMR spectra of compound **2**.

Figure S27. ^{1}H NMR spectra of compound **3**.

Figure S28. ^{1}H NMR spectra of compound **4**.

Figure S29. ^{1}H NMR spectra of compound **5**.

Figure S30. ^{13}C NMR spectra of compound **5**.

Figure S31. ^{19}F NMR spectra of compound **5**.

Figure S32. ^{11}B NMR spectra of compound **5**.

Figure S33. HRMS spectra of compound **5**.

Figure S34. FT-IR spectra of compound **5**.

Figure S35. ^{1}H NMR spectra of compound **6**.

Figure S36. ^{13}C NMR spectra of compound **6**.

Figure S37. ^{19}F NMR spectra of compound **6**.

Figure S38. ^{11}B NMR spectra of compound **6**.

Figure S39. HRMS spectra of compound **6**.

Figure S40. FT-IR spectra of compound **6**.

Materials

4,4'-Oxybis(methoxybenzene) (99%, Adamas), 3'-methoxyacetophenone (99%, Adamas), anisole (99%, Aladdin), 1,2-dimethoxybenzene (97%, Bidepharm), 3',4',5'-trimethoxyacetophenone (98%, Innochem), 2,6-dimethoxynaphthalene (98%, Anage), acetic anhydride (98.5%, Sinopharm Chemical Reagent), boron trifluoride diethyl etherate (98%, TCI), phenyl benzoate (PhB) (99%, Energy Chemical), 4-methoxybenzophenone (MeOBP) (99%, Innochem), blue up-conversion materials (Shenzhen Orient Color Change Technology Co. Ltd.)

Synthesis of compound 1 via cascade reaction

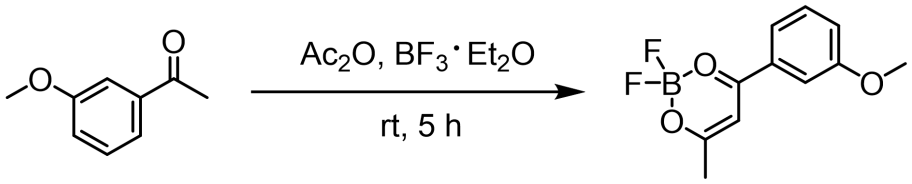

3'-methoxyacetophenone 1

Into a round bottom flask were added 3'-methoxyacetophenone (0.137 mL, 1.0 mmol), acetic anhydride (2 mL) and boron trifluoride diethyl etherate (0.62 mL, 5.1 mmol). The reaction mixture was stirred for 5 hours at room temperature. The reaction mixture was extracted with dichloromethane and washed with deionized water. The crude product was dried on anhydrous magnesium sulfate, concentrated by rotary evaporation. The crude product purified by column chromatography over silica gel using petroleum ether/dichloromethane (1:1) to give pale yellow compound **1** with an isolation yield of 64%. The compound **1** was further purified by three cycles of recrystallization in spectroscopic grade dichloromethane/hexane. ^{1}H NMR (400 MHz, Chloroform-*d,* relative to Me_4Si/ppm) δ 7.61 (d, J = 7.8 Hz, 1H), 7.58 (d, J = 2.2 Hz, 1H), 7.43 (t, J = 8.0 Hz, 1H), 7.23 (dd, J = 8.3, 1.9 Hz, 1H), 6.56 (s, 1H), 3.89 (s, 3H), 2.43 (s, 3H).

Synthesis of compound 2 via cascade reaction

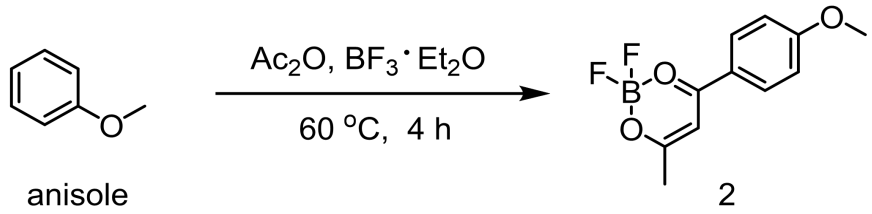

Into a round bottom flask were added anisole (0.2 mL, 1.84 mmol), acetic anhydride (2 mL) and boron trifluoride diethyl etherate (1.2 mL, 9.7 mmol). The reaction mixture was heated to 60 °C for 4 hours and cooled to room temperature. The reaction mixture was extracted with dichloromethane and washed with deionized water. The crude product was dried on anhydrous magnesium sulfate, concentrated by rotary evaporation. The crude product purified by column chromatography over silica gel using petroleum ether/dichloromethane (2:1) to give pale yellow compound **2** with an isolation yield of 75%. The compound **2** was further purified by three cycles of recrystallization in spectroscopic grade dichloromethane/hexane. ^{1}H NMR (400 MHz, Chloroform-*d,* relative to Me_4Si/ppm) δ 8.07 (d, *J* = 2.0 Hz, 1H), 8.05 (d, *J* = 2.1 Hz, 1H), 7.01 (s, 1H), 6.99 (s, 1H), 6.47 (s, 1H), 3.92 (s, 3H), 2.37 (s, 3H).

Synthesis of compound 3 via cascade reaction

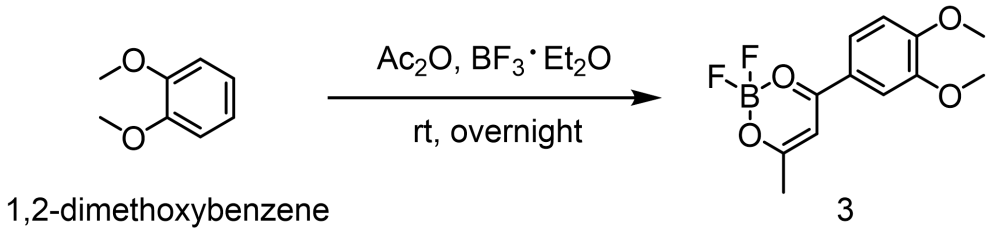

Into a round bottom flask were added 1, 2-dimethoxybenzene (0.127 mL, 1.0 mmol), acetic anhydride (2 mL) and boron trifluoride diethyl etherate (0.62 mL, 5.1 mmol). The reaction mixture was stirred overnight. The reaction mixture was extracted with dichloromethane and washed with deionized water. The crude product was dried on anhydrous magnesium sulfate, concentrated by rotary evaporation. The crude product purified by column chromatography over silica gel using

dichloromethane to give yellow compound **3** with an isolation yield of 51%. The compound **3** was further purified by three cycles of recrystallization in spectroscopic grade dichloromethane/hexane. ^{1}H NMR (400 MHz, Chloroform-*d,* relative to Me_4Si/ppm) δ 7.70 (dd, *J* = 8.6, 2.2 Hz, 1H), 7.60 (d, *J* = 2.2 Hz, 1H), 6.96 (d, *J* = 8.6 Hz, 1H), 6.48 (s, 1H), 4.00 (s, 3H), 3.97 (s, 3H), 2.39 (s, 3H).

Synthesis of compound 4 via cascade reaction

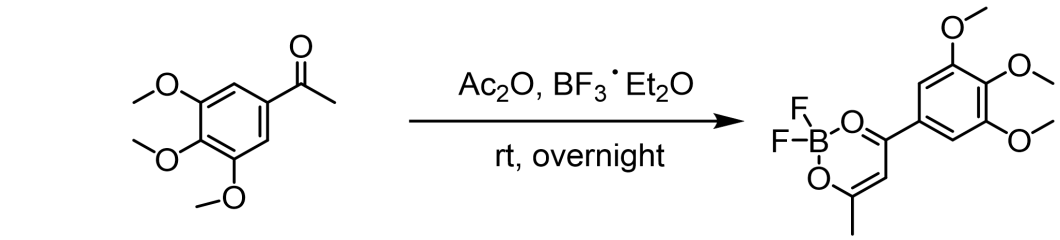

3',4',5'-trimethoxyacetophenone 4

Into a round bottom flask were added 3',4',5'-trimethoxyacetophenone (210.3 mg, 1.0 mmol), acetic anhydride (2 mL) and boron trifluoride diethyl etherate (0.62 mL, 5.1 mmol). The reaction mixture was stirred overnight. The reaction mixture was extracted with dichloromethane and washed with deionized water. The crude product was dried on anhydrous magnesium sulfate, concentrated by rotary evaporation. The crude product purified by column chromatography over silica gel using petroleum ether/dichloromethane (1:2) to give pale yellow compound **4** with an isolation yield of 52%. The compound **4** was further purified by three cycles of recrystallization in spectroscopic grade dichloromethane/hexane. ^{1}H NMR (400 MHz, Chloroform-*d,* relative to Me_4Si/ppm) δ 7.29 (s, 2H), 6.49 (s, 1H), 3.99 (s, 3H), 3.95 (s, 6H), 2.42 (s, 3H).

Synthesis of compounds 5 and 6 via cascade reaction

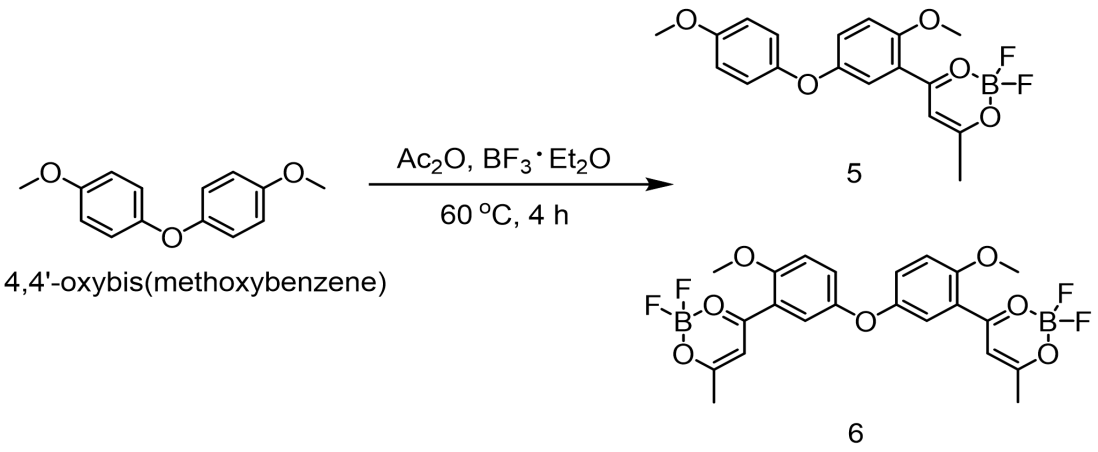

Into a round bottom flask were added 4,4'-oxybis(methoxybenzene) (796 mg, 3.46 mmol), acetic anhydride (4 mL) and boron trifluoride diethyl etherate (2.2 mL, 17.8 mmol). The reaction mixture was heated to 60 °C for 4 hours and cooled to room temperature. The reaction mixture was extracted with dichloromethane and washed with deionized water. The crude product was dried on anhydrous magnesium sulfate, concentrated by rotary evaporation. The crude product purified by column chromatography over silica gel using petroleum ether/dichloromethane (2:1) as eluent to give pale yellow (compound **5**) and orange-yellow solids (compound **6**).

The compound **5** was further purified by three cycles of recrystallization in spectroscopic grade dichloromethane/hexane (CCDC 2196201). ^{1}H NMR (400 MHz, Chloroform-*d,* relative to Me_4Si/ppm) δ 7.78 (d, *J* = 3.2 Hz, 1H), 7.23 (d, *J* = 9.1, 3.2 Hz, 1H), 7.06 (s, 1H), 6.97 (d, *J* = 9.1 Hz, 1H), 6.94 – 6.89 (m, 2H), 6.89 – 6.84 (m, 2H), 3.96 (s, 3H), 3.81 (s, 3H), 2.39 (s, 3H). ^{13}C NMR (101 MHz, Chloroform-*d*) δ 192.55, 179.85, 156.57, 155.89, 151.94, 150.48, 126.59, 121.01, 120.83, 119.88, 115.02, 113.18, 102.45, 56.29, 55.67, 24.92. ^{19}F NMR (376 MHz, Chloroform-*d,* 298 K, relative to $CFCl_3$ /ppm) δ -138.62, -138.68. ^{11}B NMR (128 MHz, Chloroform-*d*, 298 K, relative to $BF_3{\cdot}Et_2O$ /ppm) δ -0.11. FT-IR (KBr, cm^{-1}): ν 3166.5, 3091.5, 3042.9, 3014.9, 2973.5, 2951.1, 2915.7, 2842.8, 1532.1, 1506.8, 1490.0, 1466.5, 1444.1, 1424.6, 1367.6, 1343.1, 1299.8, 1271.9, 1256.1, 1171.9, 1158.9, 1091.1,

1075.9, 1051.0, 1031.5, 1010.6, 978.6, 962.1, 884.4, 863.6, 841.6, 829.6, 802.7, 772.4, 743.3, 705.8, 649.0, 619.2, 575.2,549.2, 525.0. HRMS m/z found (calcd for $C_{18}H_{17}O_5BF_2NH_4^+$): 379.1515 (379.1512).

The compound **6** was further purified by three cycles of recrystallization in spectroscopic grade dichloromethane/hexane (CCDC 2196202). ^{1}H NMR (400 MHz, Chloroform-*d,* relative to Me_4Si/ppm) δ 7.69 (s, 2H), 7.29 (d, *J* = 12.2 Hz, 2H), 7.08 (s, 2H), 7.03 (s, 2H), 3.99 (s, 6H), 2.40 (s, 6H). ^{13}C NMR (101 MHz, Chloroform-*d*) δ 192.80, 179.54, 121.24, 120.99, 113.48, 56.31. ^{19}F NMR (376 MHz, Chloroform-*d,* 298 K, relative to $CFCl_3$ /ppm) δ -138.55, -138.61. ^{11}B NMR (128 MHz, Chloroform-*d,* relative to $BF_3{\cdot}Et_2O$ /ppm) δ 0.37. FT-IR (KBr, cm^{-1}): ν 3168.8, 3083.6, 3022.8, 2948.0, 2845.2, 1532.2, 1488.6, 1465.6, 1421.2, 1366.5, 1336.5, 1268.8, 1218.9, 1170.5, 1143.2, 1095.2, 1053.2, 1015.7, 971.1, 908.8, 890.0, 826.1, 779.8, 742.8, 708.4, 655.0, 635.1, 609.3, 574.0, 547.5, 507.3. HRMS m/z found (calcd for $C_{22}H_{20}O_7B_2F_4NH_4^+$): 510.1741 (510.1742).

Preparation of afterglow materials by doping BF_2bdk into organic matrices

For the preparation of BF_2bdk-PhB-0.01% powders, 100 μL BF_2bdk in dichloromethane (0.1 mg/mL) and 100 mg phenyl benzoate (PhB) were added into an agate mortar (diameter = 5 cm). After grinding and solvent evaporating, BF_2bdk-PhB-0.01% powders that show afterglow properties were obtained. Other afterglow materials in this study at different doping concentrations, using different BF_2bdk compounds and different organic matrices were prepared through similar processes.

For the preparation of BF_2bdk-PhB-0.01% melt-cast materials, 100 μL BF_2bdk in dichloromethane (0.1 mg/mL) and 100 mg phenyl benzoate (PhB) were added into a 3 mL sample bottle, and then heated to 80 °C to give a molten mixture. Subsequently, the sample bottle was transferred to a bath of liquid nitrogen to immediately solidify the molten mixture. After standing at room temperature for tens of minutes, melt-cast BF_2bdk-PhB-0.01% afterglow materials were obtained. Other afterglow materials at different doping concentrations, using different BF_2bdk compounds and different organic matrices were prepared through similar processes.

Physical measurements and instrumentation

Nuclear magnetic resonance (NMR) spectra were recorded on a JEOL Fourier-transform NMR spectrometer (400 MHz), including ^{1}H NMR, $^{13}C\{^{1}H\}$ NMR, $^{19}F\{^{1}H\}$ NMR, $^{11}B\{^{1}H\}$ NMR. Mass spectra were performed on Agilent Technologies 5973N and Thermo Fisher Scientific LTQ FT Ultras mass spectrometer. FT-IR spectra were recorded on a Nicolet AVATAR-360 FT-IR spectrophotometer with a resolution of 4 cm^{-1}. X-Ray diffraction data of the crystals were collected using synchrotron radiation (λ = 0.82652 Å) on beamline 17B at the National Facility for Protein Science Shanghai (NFPS) in the Shanghai Synchrotron Radiation Facility, People's Republic of China. The diffraction data reduction and integration were performed by the HKL3000 software. The structures were solved by direct methods and refined employing full-matrix least-squares on F2 by using SHELXL program through the OLEX2 interface (Sheldrick G, Crystal Structure Refinement with SHELXL. *Acta. Crystallogr. Sect. C* 2015, 71: 3-8; Dolomanov OV, Bourhis L J, Gildea R J, Howard JAK and Puschmann H, OLEX2: A Complete Structure Solution, Refinement and Analysis Program. *J. Appl. Crystallogr.* 2009, 42: 339-341). All non-H atoms of the compounds were refined with anisotropic thermal parameters. The hydrogen atoms were included in idealized positions and refined with fixed geometry with respect to their carrier atoms. Refinement data of the compounds was processed by using SQUEEZE program (Spek A, Single-crystal Structure Validation with the Program PLATON. *J. Appl. Crystallogr.* 2003, 36: 7-13). The X-ray crystallographic data for the compounds has been deposited at the Cambridge Crystallographic Data Centre (CCDC), under the deposition number CCDC 2196201 (compound **5**) and 2196202 (compound **6**). UV-Vis absorption spectra were recorded on a Techcomp UV1050 UV-vis spectrophotometer. The steady-state and delayed emission spectra were collected by Hitachi FL-4700 fluorescence spectrometer equipped with chopping systems; the delayed emission spectra were obtained with a delay time of approximately 1 ms. The excited state decay profiles in millisecond to second region were collected by Hitachi FL-4700 fluorescence spectrometer equipped with chopping systems. It is noted that Figure 3B and 3E show the presence of 409-425 nm

signals in the delayed emission spectra when excited at 389 nm. It is found that the 409-425 nm signals disappeared in the delayed emission spectra when excited at 365 nm and 350 nm (Figure S24). The 409-425 nm signals in Figure 3B and 3E are originated from the light scattering of the excitation source. Although the excitation wavelength is set at 389 nm, the excitation source is not a real monochromator but has a certain wavelength distribution. Due to light scattering, the lower-energy part of the excitation source would enter the spectrograph slit during the illuminating phase of the Hitachi FL-4700 phosphoroscope rotation, giving rise to the 409-425 nm signals. The signals of these scattered excitation lights are weak so that these signals have insignificant influence to the delayed emission spectra of 5-PhB-0.01% materials at 77 K where nonradiative decay of triplet states are well suppressed. However, at room temperature or even higher temperature, the delayed emission intensities of 5-PhB-0.01% materials decrease and become weak, so that one can observe the coexistence of the 409-425 nm signals of the scattered excitation lights in the delayed emission spectra. The fluorescence decay profiles in nanosecond region were recorded by using time-correlated single photon counting technique (TCSPC) on a Edinburgh FLS1000 fluorescence spectrometer equipped with a picosecond pulsed diode laser. Photoluminescence quantum yield was measured by a Hamamatsu absolute PL quantum yield measurement system based on a standard protocol (*Adv. Mater.* 1997, 9: 230). Photographs and videos were captured by HUAWEI P30 cameras. Before the capture, samples were irradiated by a 365 nm UV lamp (5 W) for approximately 5 s at a distance of approximately 15 cm.

TD-DFT calculations

TD-DFT calculations were performed to study the photophysical properties of molecularly dispersed BF_2bdk in the solid state. Since the afterglow properties are originated from the excited states of molecularly dispersed BF_2bdk in the rigid PhB matrices where intermolecular rotation and vibration are largely restricted, the

ground-state geometry of BF_2bdk was used for all the TD-DFT calculations. The ground-state geometry of compounds **1**-**4** were optimized by a DFT calculation using B3LYP functional and 6-31G (d, p) basis set. The ground-state geometry of compounds **5** and **6** were obtained from their single crystal structure. The singlet excited states and triplet excited states were calculated on Gaussian 16 program (Revision A.03) with B3LYP functional and 6-31G (d, p) basis set. Spin-orbit coupling (SOC) matrix elements between the singlet excited states and triplet excited states were calculated with spin-orbit mean-field (SOMF) methods on ORCA 4.2.1 program with B3LYP functional and def2-TZVP(-f) basis set. The obtained electronic structures were analyzed by Multiwfn software. All isosurface maps to show the electron distribution and electronic transitions were rendered by Visual Molecular Dynamics (VMD) software based on the exported files from Multiwfn. The dipole moments of compound **1**-**6**'s S_1 states and PhB's ground state were calculated on Gaussian 16 program (Revision A.03) using B3LYP functional and 6-31G (d, p) basis set, and analyzed by Multiwfn software. (Neese F, *Wiley Interdiscip. Rev. Comput. Mol. Sci.* 2018, 8: 1327-1332; Becke AD, *Phys. Rev. A* 1988, 38: 3098-3100; Lee C, Yang W, Parr RG, *Phys. Rev. B.* 1988, 37: 785-789; Miehlich B, Savin A, Stoll H, Preuss H, *Chem. Phys. Lett.* 1989, 157: 200-206; Weigend F, Ahlrichs R, *Phys. Chem. Chem. Phys.* 2005, 7: 3297-3305; Lu T, Chen F, *J. Comput. Chem.* 2012, 33: 580-592; Humphrey W, Dalke A, Schulten K, *J. Mol. Graphics* 1996, 14: 33-38).

Text S1. Selection guideline of organic matrices

In the early stage of the studies on BF_2bdk-matrix systems, we prepare high-performance afterglow materials by screening BF_2bdk compounds and organic matrices. During the studies in recent two years, we do accumulate some knowledge on the selection guideline of the organic matrices in our BF_2bdk-matrix systems. (1) Organic matrices with relatively large dipole moments can interact with BF_2bdk excited states via dipole-dipole interactions, reduce S_1 levels of BF_2bdk (T_1 levels of BF_2bdk is relatively insensitive to medium or environment), and thus decrease ΔE_{ST} values and enhance both ISC and RISC. Because of their relatively large dipole moments, benzophenone derivatives can be used as suitable organic matrices for the fabrication of BF_2bdk-matrix afterglow materials in some circumstance. (2) To suppress afterglow quenching caused by excited state energy transfer from BF_2bdk triplets to organic matrices, organic matrices with higher T_1 levels than BF_2bdk is necessary for the fabrication of high-performance afterglow materials in our BF_2bdk-matrix systems. In the case of BF_2bdk with low T_1 levels, it is found that benzophenone derivatives such as BP and MeOBP can be suitable organic matrices. When the BF_2bdk dopants possess high T_1 levels, phenyl benzoate (PhB) can be suitable matrices due to their higher T_1 levels (benzophenone derivatives is not suitable as reported in *Angew. Chem. Int. Ed.* **2021**, 60, 17138 and *Chem. Commun.* **2021**, *57*, 8794). (3) It is also found that organic matrices such as phenyl benzoate and benzophenone derivatives can protect BF_2bdk triplets from oxygen quenching and largely suppress nonradiative decay of BF_2bdk triplets, especially in the melt-cast

dopant-matrix afterglow materials (*Adv. Opt. Mater.* **2021**, 2100353; *Chem. Commun.* **2021**, *57*, 8794). Based on the above knowledge, it is understandable that, since the BF_2bdk in the present study possess relatively high T_1 levels, PhB matrices, rather than benzophenone derivatives, are selected for the fabrication of afterglow materials.

Text S2. Rule out some afterglow mechanisms.

Excited state energy transfer from RTP donors to luminescent acceptors has been reported to give rise to organic afterglow at room temperature (*Nat. Commun.* **2020**, *11*, 4802; *Angew. Chem. Int. Ed.* **2020**, *59*, 9393). The excited state energy transfer only occurs when the donors are sufficiently excited. In the present study, the afterglow emission of BF_2bdk-PhB-0.01% samples can be excited by 365 nm UV. Since PhB matrices possess negligible UV-vis no absorption at 365 nm, the possibility of excited state energy transfer from PhB matrices to BF_2bdk for the emergence of room-temperature afterglow can be ruled out.

In some reported organic systems (*Nature* **2017**, *550*, 384), the donor-acceptor mechanism possess charge-separated states within the organic materials. The retarded charge recombination in the rigid solid medium is responsible for the long persistent luminescence in organic systems. Intermolecular charge transfer in donor-acceptor systems can lead to the formation of charge-separated states, which is a prerequisite for the organic long persistent luminescence properties in donor-acceptor afterglow systems. In the present study, since the organic matrices such as PhB possess low-lying HOMOs and high-lying LUMOs when compared to BF_2bdk dopants, intermolecular charge transfer between dopants and matrices would be insignificant in

the present system and thus the organic long persistent luminescence mechanism can be ruled out.

It has been reported recently that isomeric impurity is responsible for the emergence of organic room-temperature afterglow in carbazole systems (*Nat. Mater.* **2021**, 20, 175). In the present study, BF_2bdk powders show no afterglow properties at room temperature. The BF_2bdk compounds were purified by careful column chromatography followed by recrystallization in spectroscopic grade dichloromethane/*n*-hexane for three times. HPLC measurement confirms its high purity. Upon doping into PhB matrices, BF_2bdk-PhB-0.01% samples exhibited significant afterglow properties under ambient conditions. When dispersed in organic matrices at low doping concentration such as 0.01 wt%, the BF_2bdk molecules and the possible impurities should be separated by organic matrices, so charge separation and recombination processes between BF_2bdk molecules and the possible impurities are statistically negligible. These experiments and analysis can rule out the possibility that the room-temperature afterglow of BF_2bdk-PhB-0.01% materials is originated from some impurities.

Recent studies in the literature showed that triplet excited states of organic matrices with energy levels sandwiched between S_1 and T_1 states of phosphorescence dopants can mediate singlet-to-triplet ISC of the phosphorescence dopants, leading to the emergence of room-temperature afterglow (*Angew. Chem. Int. Ed.* **2020**, *59*, 16054). This mediation of ISC is not the case in the present BF_2bdk-PhB system because T_1 level of PhB matrices is much higher than both the S_1 and T_1 states of

fluoreneBF$_2$ molecules. Actually, according to the studies by Adachi's group and us, high T_1 levels of organic matrices are very important for the fabrication of high-performance afterglow materials since it can avoid afterglow quenching caused by triplet-to-triplet energy transfer from luminescent dopants to organic matrices (*Adv. Funct. Mater.* **2013**, *23*, 3386; *Angew. Chem. Int. Ed.* **2021**, *60*, 17138).

Text S3. Difference between conventional TADF emitters and TADF afterglow emitters

Given that the RISC process is the rate-determining step for TADF, the k_{RISC} value in the present TADF-afterglow system can be estimated from the afterglow lifetimes, that is, the TADF lifetime, to be on the order of 10^0-10^1 s^{-1}. It is worth mentioning that the requirements on k_{RISC} values for TADF-type afterglow materials are different from those for efficient TADF-based OLED devices. TADF emitters with large k_{RISC} values on the order of 10^3-10^6 s^{-1} are necessary to fabricate efficient OLED devices. It has been reported that usually organic molecular systems should meet two conditions simultaneously to achieve large k_{RISC}: (1) small ΔE_{ST} values, for example, smaller than 0.2 eV; (2) large spin-orbit coupling matrix elements (SOCME) (*J. Am. Chem. Soc.* **2017**, *139*, 4042; *J. Am. Chem. Soc.* **2012**, *134*, 14706; *Adv. Sci. (Weinh)* **2016**, *3*, 1600080; *Sci. Adv.* **2018**, *4*, eaao6910). In the absence of heavy atom effect (HAE), relatively large SOCME can be realized by incorporating triplet excited states of different excited state nature from the lowest singlet excited states according to the El-Sayed rule. We reason that if organic molecular systems meet

condition (1), or meet condition (2), or partially meet condition (1) and (2), a moderate k_{RISC} value on the order of 10^{-1}-10^{2} s^{-1} can be obtained. Given that k_P values in ordinary organic systems in the absence of HAE is on the order of 10^{-2}-10^{3} s^{-1}, such a moderate k_{RISC} value is considered to be suitable to open a TADF pathway to harvest the energy of triplet excited states. Most conventional LE molecules possess very small k_{RISC} values due to the large ΔE_{ST} values and small SOCME. The BF_2bdk molecules of intramolecular charge transfer characters possess much smaller singlet-triplet splitting energy than LE systems, which enhance intersystem crossing to a large extent. TD-DFT calculations show that there are rich ISC and RISC channels with SOCME values around 1 cm^{-1} and above. Furthermore, the dipole-dipole interactions between BF_2bdk' ^{1}ICT states and PhB matrices facilitate ISC and RISC. In view of these, it is understandable that the present BF_2bdk-PhB system can obtain a moderate k_{RISC} on the order of 10^{0} to 10^{1} s^{-1} and possess TADF-type organic afterglow mechanism; k_P values of the F_2bdk-PhB systems should be much smaller than k_{RISC} at room temperature. Overall, the present study and the related reported studies (*Angew. Chem. Int. Ed.* **2021**, *60*, 17138; *Adv. Funct. Mater,* **2021**, 2110207; *Chem. Eng. J.* **2022**, *431*, 134197) suggest that the requirement to obtain moderate k_{RISC} of 10^{-1}-10^{2} s^{-1} by either small ΔE_{ST} or large SOCME should be less stringent than that of TADF emitter for efficient OLED. These are our understanding on the difference of k_{RISC} and molecular design between conventional TADF emitters and TADF afterglow emitters.

Text S4. Advancement of the present TADF-type organic afterglow system

Compared to our previous studies on TADF-type organic afterglow, there are at least three differences and advancements in the present study. (1) The present study provides a rational design on TADF-type organic afterglow systems, which would evolve into a general strategy for TADF afterglow. Specifically, the HOMO-LUMO separation in charge transfer systems reduce ΔE_{ST}, the dipole effect further decrease ΔE_{ST}, and the multiple donor design and twisted molecular design enhance SOCME. These charge transfer design and dopant-matrix strategy can be readily extended to other organic systems, so that the present study provides a rational and general pathway for TADF-type organic afterglow materials. (2) With the aid of up-conversion materials, the TADF afterglow systems achieve NIR excitable properties, which has not been reported in our previous TADF afterglow systems and would be very important for the promising biomedical applications of these materials. (3) The TADF afterglow materials feature singlet afterglow properties, small Stokes shifts and high efficiency. These unique properties of TADF-type afterglow materials, when compared to room-temperature phosphorescence materials, have been first described and pointed out in the present study.

Table S1. Photophysical data of BF_2bdk compounds at room temperature.

Entry	λ_{abs}/nm ($\varepsilon \times 10^{-4}$/$M^{-1}cm^{-1}$)	λ_{em}/nm	τ/ns
5 in dichloromethane	388 (0.84)	505	τ_1 = 2.15 (79.87%) τ_2 = 11.11 (20.13%)
5 in ethyl acetate	382 (0.80)	487	τ_1 = 0.70 (45.16%) τ_2 = 4.96 (54.84%)
5 in acetone	385 (0.94)	491	τ_1 = 0.54 (53.78%) τ_2 = 3.25 (46.22%)
5 in tetrahydrofuran	382 (0.82)	490	τ_1 = 0.43 (40.65%) τ_2 = 5.61 (59.35%)
6 in dichloromethane	382 (1.56)	504	τ = 2.05
6 in ethyl acetate	372 (1.63)	493	τ_1 = 0.68 (44.13%) τ_2 = 4.70 (55.87%)
6 in acetone	381 (2.12)	509	τ_1 = 0.54 (48.04%) τ_2 = 3.11 (51.96%)
6 in tetrahydrofuran	378 (3.04)	497	τ_1 = 0.46 (45.03%) τ_2 =5.35 (54.97%)

Table S2. Calculation results of dipole moments of BF_2bdk molecules' S_1 states.

Entry	S_1-Dipole Moment/Debye
Compound **1**	17.56
Compound **2**	15.92
Compound **3**	19.44
Compound **4**	17.08
Compound **5**	20.49
Compound **6**	19.25

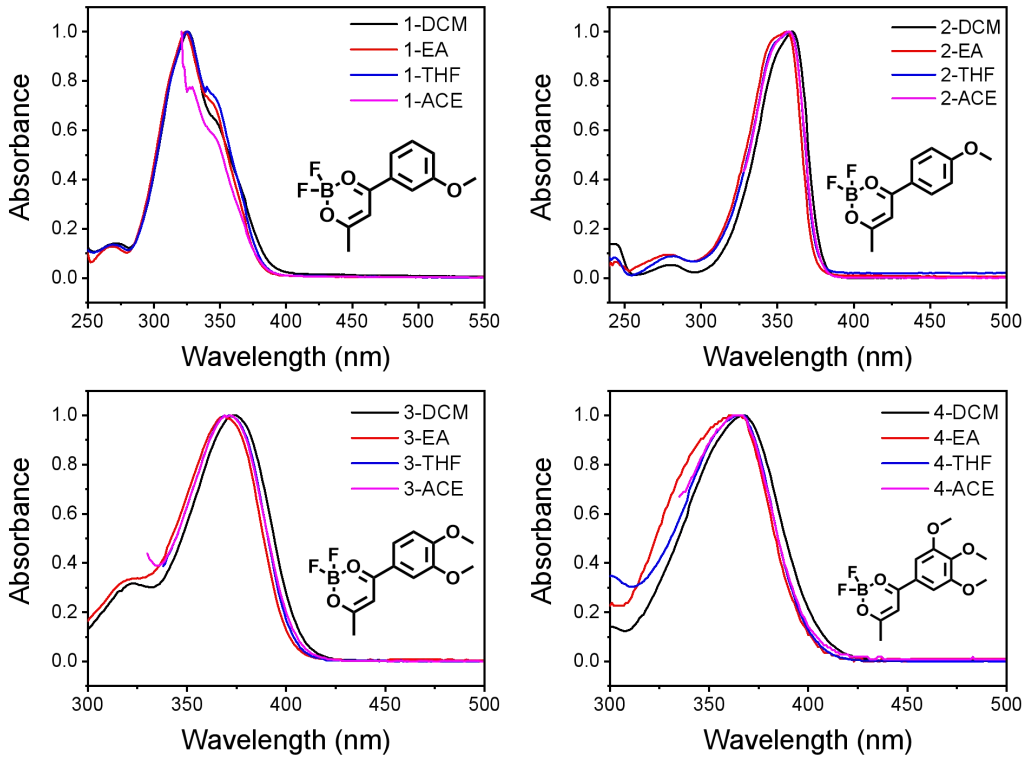

Figure S1. UV-vis spectra of BF_2bdk in different solvents. DCM, EA, THF and ACE refer to dichloromethane, ethyl acetate, tetrahydrofuran and acetone, respectively.

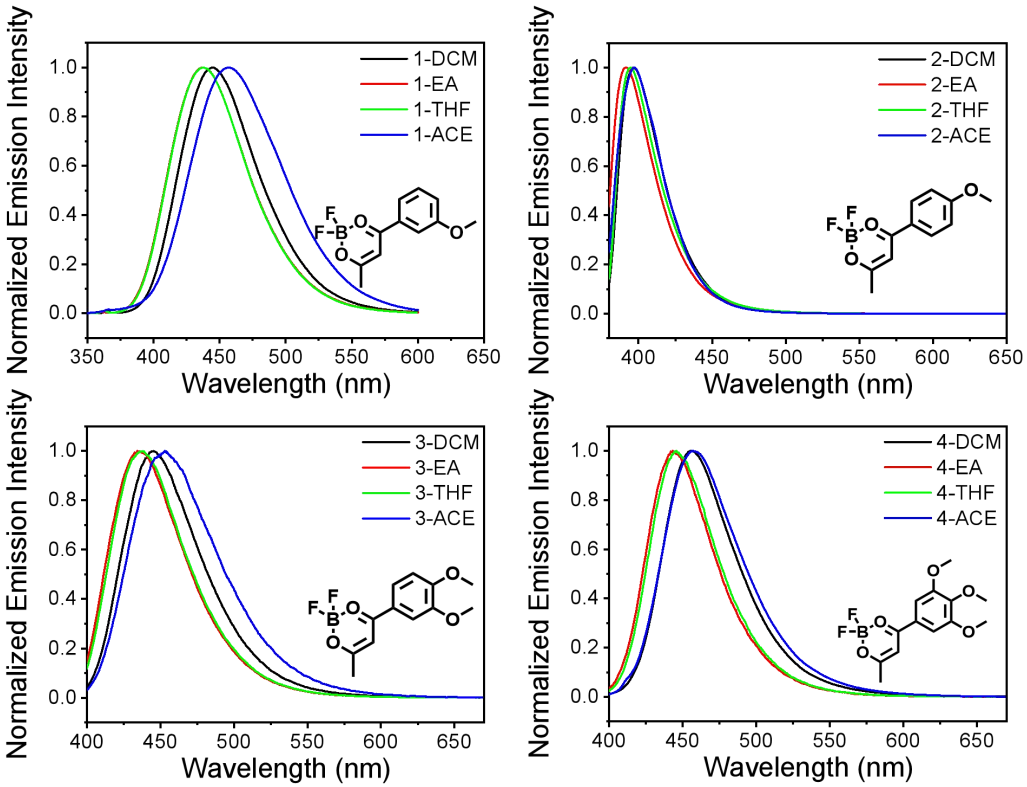

Figure S2. Room-temperature steady-state emission spectra of BF_2bdk in different solvents. DCM, EA, THF and ACE refer to dichloromethane, ethyl acetate, tetrahydrofuran and acetone, respectively. According to the studies by Lippert and Mataga (*Elektrochem.* **1957**, *61*, 962-975; *Bull. Chem. Soc. Jpn.* **1956**, *29*, 465-470), the Stokes shift is proportional to the orientation polarizability, where DCM has a higher orientation polarizability than EA. Therefore, the solution emission properties of 1-4 in different solvents agree with the studies by Lippert and Mataga and other related studies (*J. Am. Chem. Soc.* **2005**, *127*, 1300-1306).

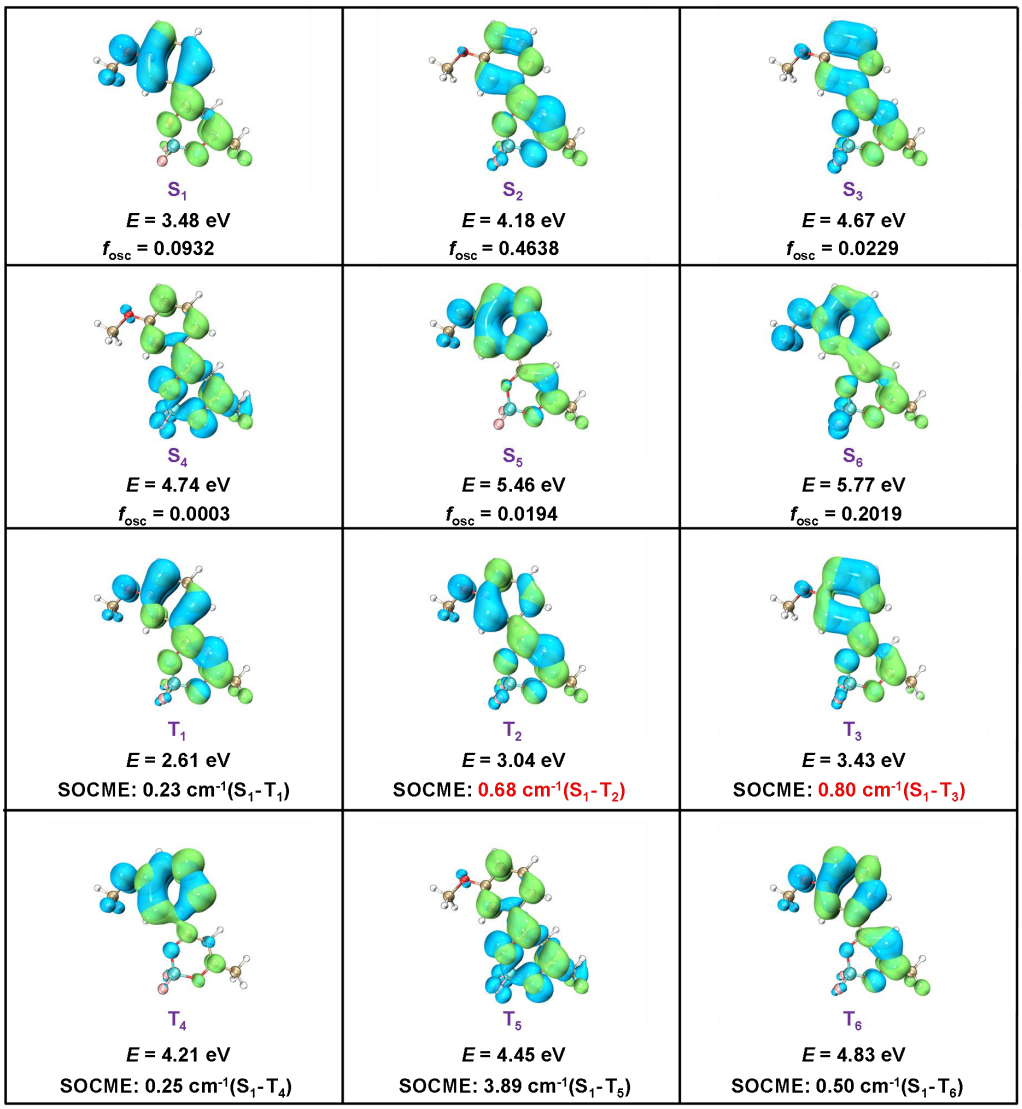

Figure S3. The TD-DFT calculated results of compound **1** singlet and triplet excited states. From the results of TD-DFT calculation, it is found that S_1 and T_1 states of compound **1** showed similar excited state symmetry, while T_2 and T_3 states showed different excited state nature from S_1 states. According to the El-Sayed rule, such different symmetry between S_1 and T_n states would enhance singlet-to-triplet intersystem crossing. The S_1-to-T_2 and S_1-to-T_3 ISC channels possess relatively small singlet-triplet energy gap and relatively large SOCME of 0.68 cm^{-1} and 0.80 cm^{-1} when compared to S_1-to-T_1 ISC channel; S_1-to-T_2 and S_1-to-T_3 ISC channels facilitate the intersystem crossing of compound **1**. This is our understanding on the singlet-to-triplet ISC in compound **1** system. With the assist of PhB matrices, the **1**-PhB-0.01% materials exhibited RTP mechanim with long emission lifetimes (other afterglow mechanisms have been ruled out in Text S2).

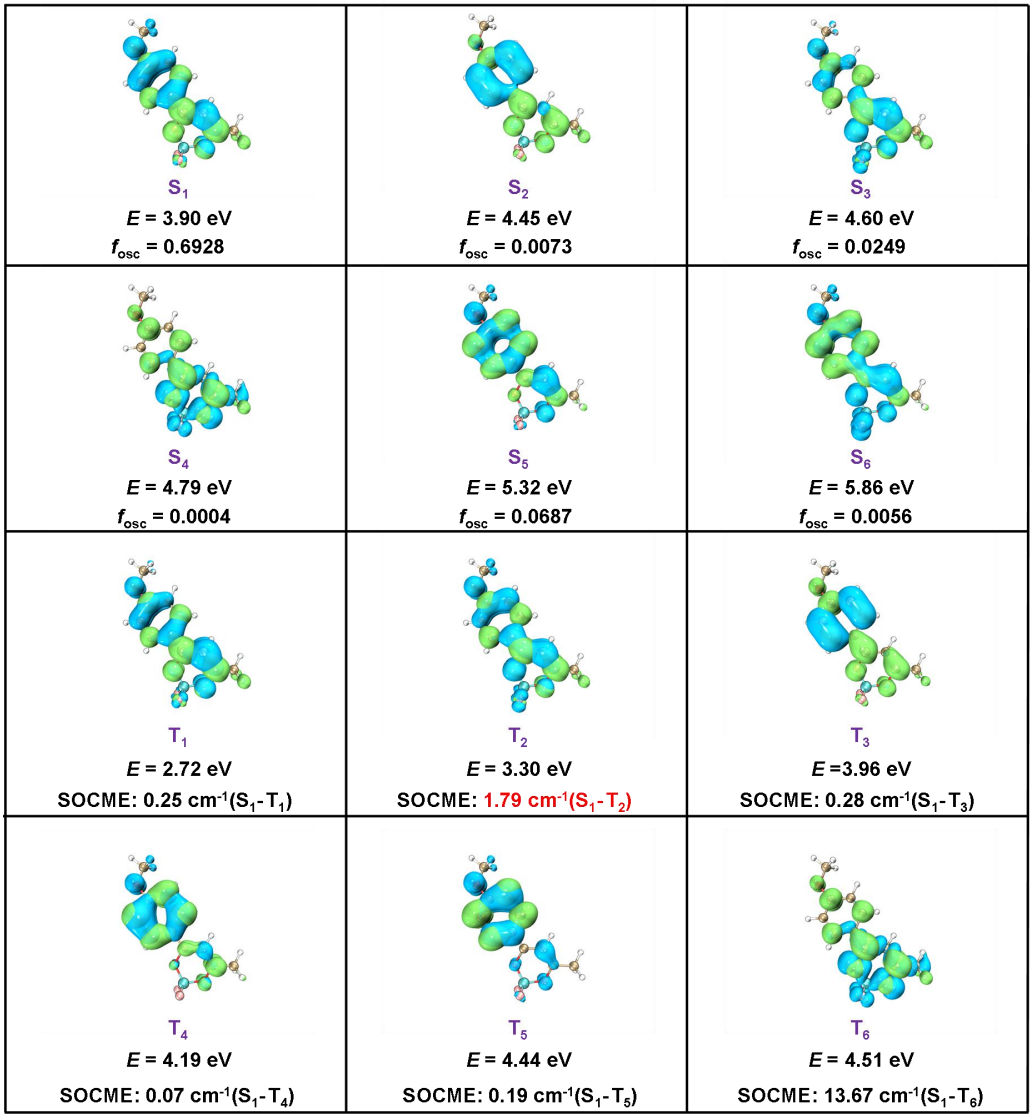

Figure S4. The TD-DFT calculated results of compound **2** singlet and triplet excited states. From the results of TD-DFT calculation, it is found that S_1 and T_1 states of compound **2** showed similar excited state symmetry, while T_2 states exhibited different excited state nature from S_1 states. According to the El-Sayed rule, such different symmetry between S_1 and T_2 states would enhance singlet-to-triplet intersystem crossing. The S_1-to-T_2 ISC channel showed relatively small singlet-triplet energy gap and relatively large SOCME of 1.79 cm^{-1} when compared to S_1-to-T_1 ISC channel; S_1-to-T_2 ISC channel facilitates the intersystem crossing of compound **2**. This is our understanding on the singlet-to-triplet ISC in compound **2** system. With the assist of PhB matrices, the **2**-PhB-0.01% materials exhibited RTP mechanim with long emission lifetimes (other afterglow mechanisms have been ruled out in Text S2).

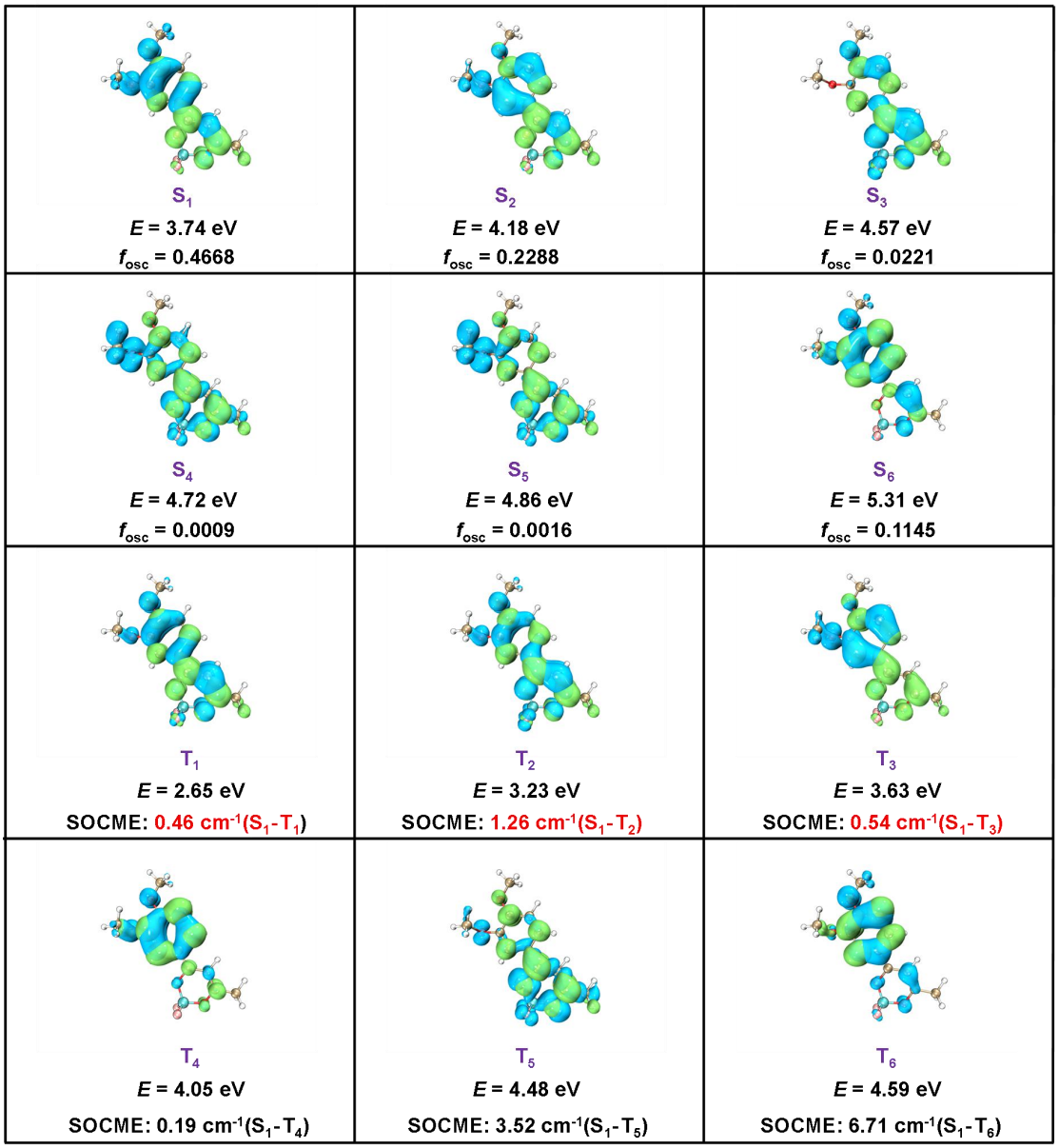

Figure S5. The TD-DFT calculated results of compound **3** singlet and triplet excited states. From the results of TD-DFT calculation, it is found S_1-to-T_1, S_1-to-T_2 and S_1-to-T_3 ISC channels possess relatively large SOCME of 0.46 cm^{-1}, 1.26 cm^{-1} and 0.54 cm^{-1}; these ISC channels facilitate the intersystem crossing of compound **3**. With the assist of PhB matrices, the **3**-PhB-0.01% materials exhibited RTP mechanim with long emission lifetimes (other afterglow mechanisms have been ruled out in Text S2).

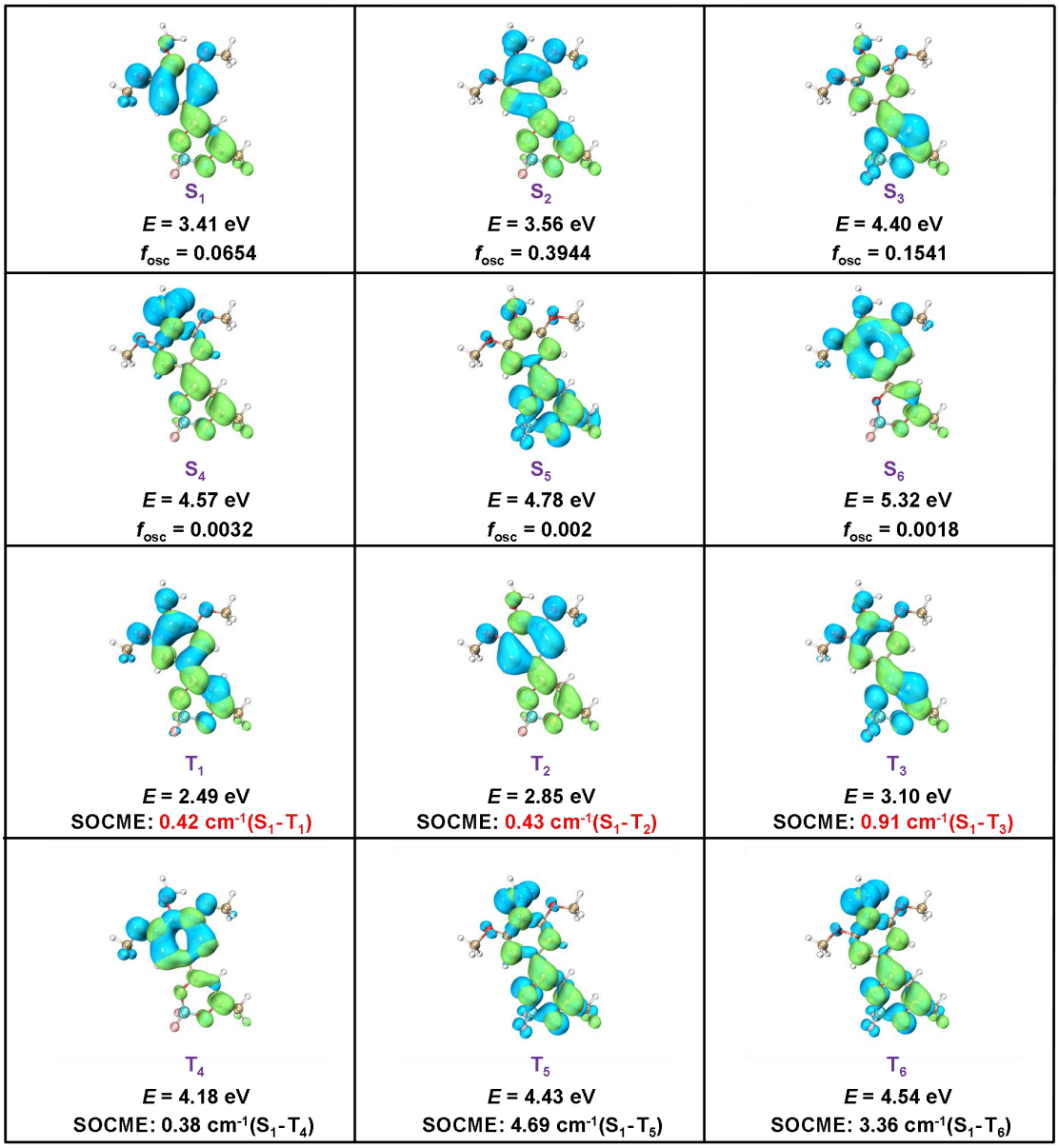

Figure S6. The TD-DFT calculated results of compound **4** singlet and triplet excited states. From the results of TD-DFT calculation, it is found S_1-to-T_1, S_1-to-T_2 and S_1-to-T_3 ISC channels possess relatively large SOCME of 0.42 cm^{-1}, 0.43 cm^{-1} and 0.91 cm^{-1}; these ISC channels facilitate the intersystem crossing of compound **4**. With the assist of PhB matrices, the **4**-PhB-0.01% materials exhibited RTP mechanim with long emission lifetimes (other afterglow mechanisms have been ruled out in Text S2).

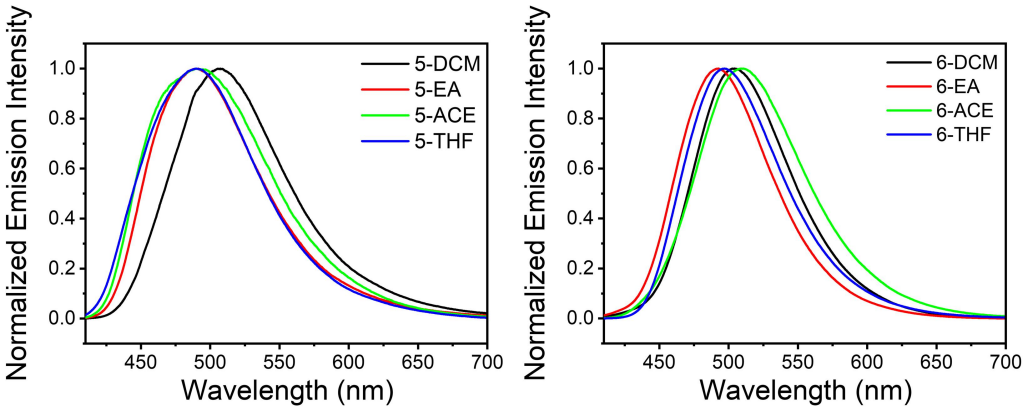

Figure S7. Room-temperature steady-state emission spectra of BF_2bdk in different solvents. DCM, EA, THF and ACE refer to dichloromethane, ethyl acetate, tetrahydrofuran and acetone, respectively.

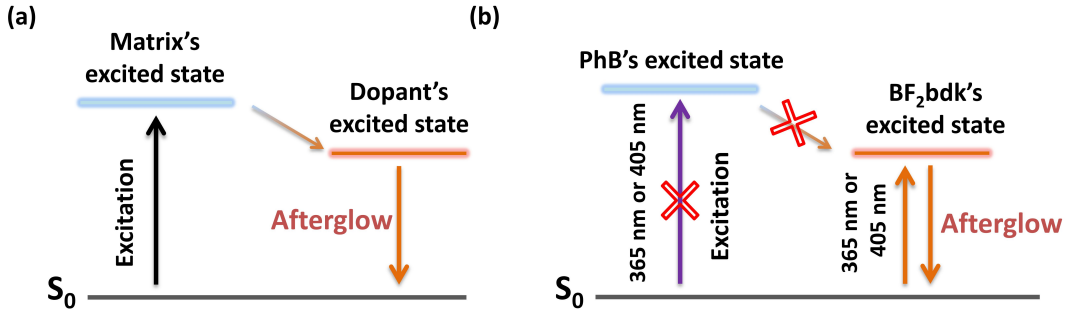

Figure S8. (a) Schematic illustration of triplet-to-singlet excited state energy transfer (TSET) from matrices to dopants in the reported studies. (b) Schematic illustration of the excited state energy levels of PhB and BF_2bdk in the present study. Significant afterglow properties in these systems can only be observed when the donors were sufficiently excited. The **5**-PhB-0.01% melt-cast material showed long-lived afterglow upon 365 nm or 405 nm excitation while PhB has negligible UV-vis absorption at 365 nm or 405 nm, so we reason that TSET is not responsible for the significant afterglow in the present system.

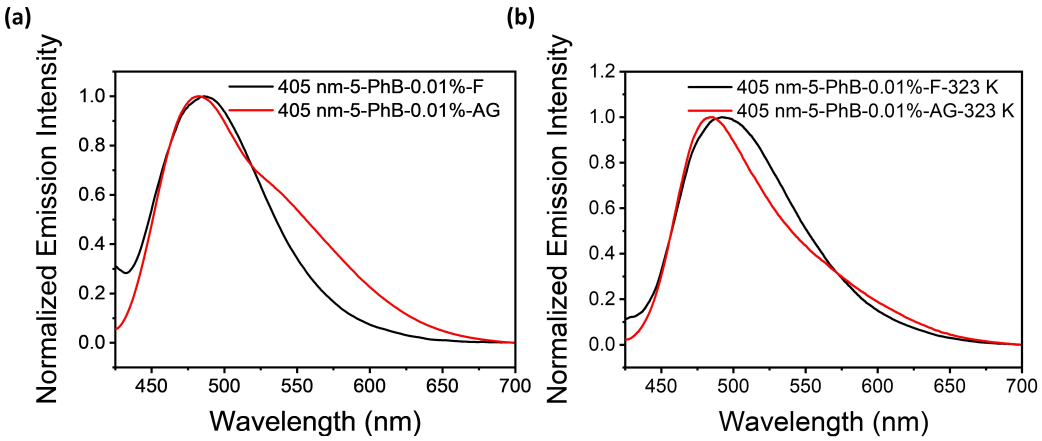

Figure S9. (a) Delayed emission (1 ms delay) spectra of 5-PhB-0.01% melt-cast materials under ambient conditions. (b) Delayed emission (1 ms delay) of 5-PhB-0.01% melt-cast materials under ambient conditions at 323 K.

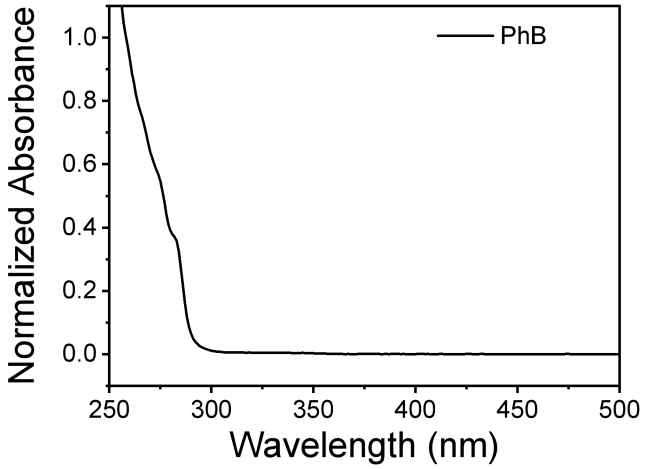

Figure S10. UV-vis spectra of PhB. TD-DFT calculations (B3LYP functional and 6-31g (D, P) basis sets) were used to estimate the HOMO (-6.96 eV), LUMO (-1.79 eV), S_1 (4.52 eV) and T_1 (3.53 eV) levels of PhB.

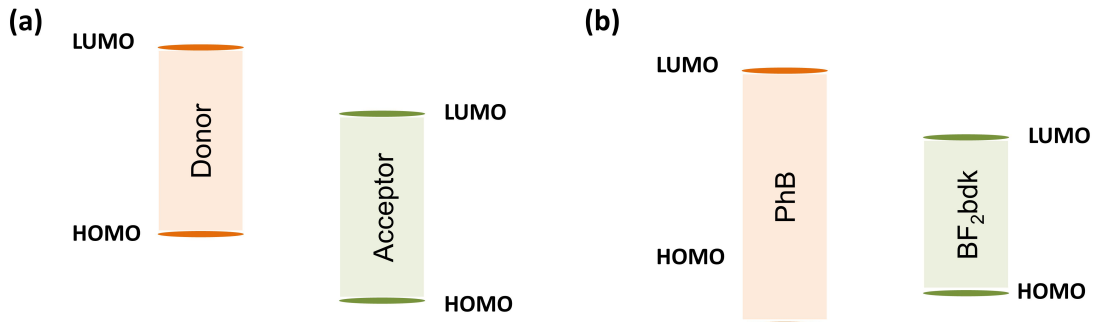

Figure S11. (a) Schematic illustration of HOMO and LUMO levels of donors and acceptors with the involvement of intermolecular charge transfer. (b) Schematic illustration of HOMO and LUMO levels of compound **5** and PhB in the present study. PhB matrices possess higher-lying LUMO and lower-lying HOMO compared to **5**. The insignificant intermolecular charge transfer in **5**-PhB materials can rule out the contribution of donor-acceptor mechanism to the present organic afterglow system.

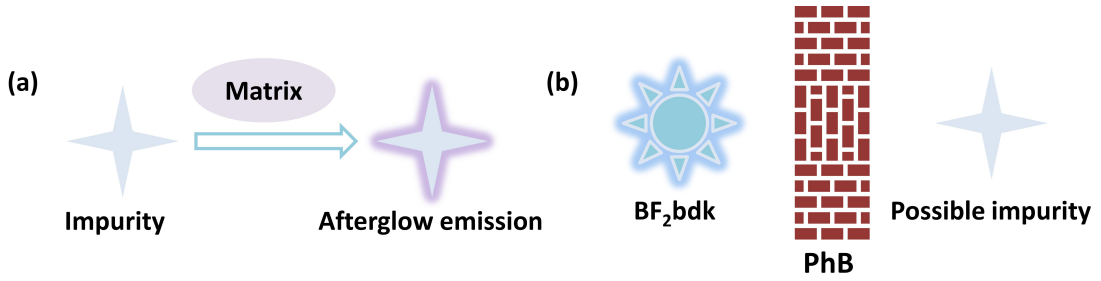

Figure S12. (a) Schematic illustration of the impurity mechanism for organic afterglow. (b) Schematic illustration of the separation of BF_2bdk and possible impurity by PhB matrices in the present study. In the present study, the high purity of **5** confirmed by HPLC measurement, as well as the similar maxima in UV-vis spectra and excitation spectra of **5**-PhB-0.01% melt-cast materials, can rule out the contribution of impurity mechanism to the present afterglow material systems.

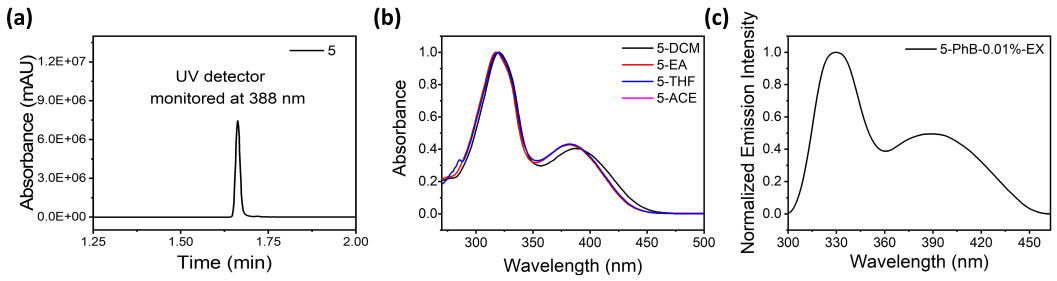

Figure S13. (a) HPLC spectrum of compound **5**. UV absorption was monitored at 388 nm. (b) UV-vis spectra of compound **5** in different solvents. DCM, EA and THF refer to dichloromethane, ethyl acetate and tetrahydrofuran, respectively. (c) Excitation spectra of **5**-PhB-0.01% samples.

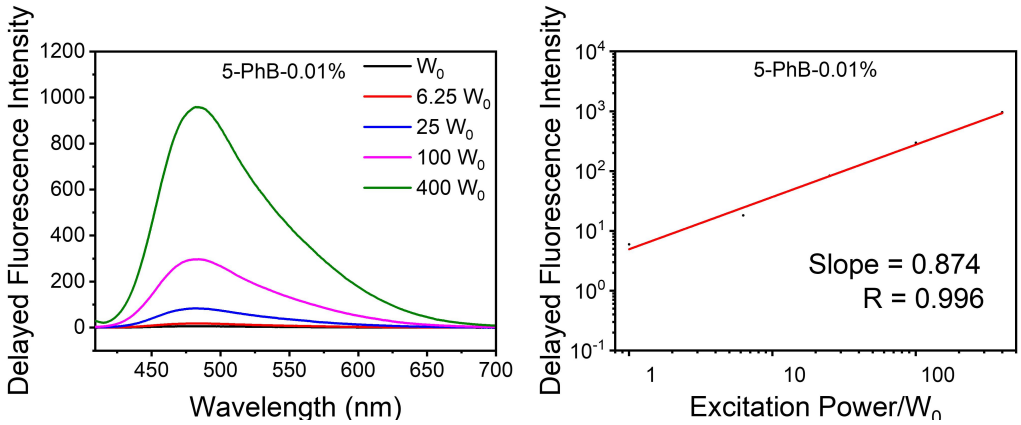

Figure S14. Power-dependent delayed fluorescence spectra of **5**-PhB-0.01% samples. It is found that the intensity of delayed fluorescence of the afterglow materials exhibit a quasi-linear dependence on the excitation dose, which further support the TADF mechanism.

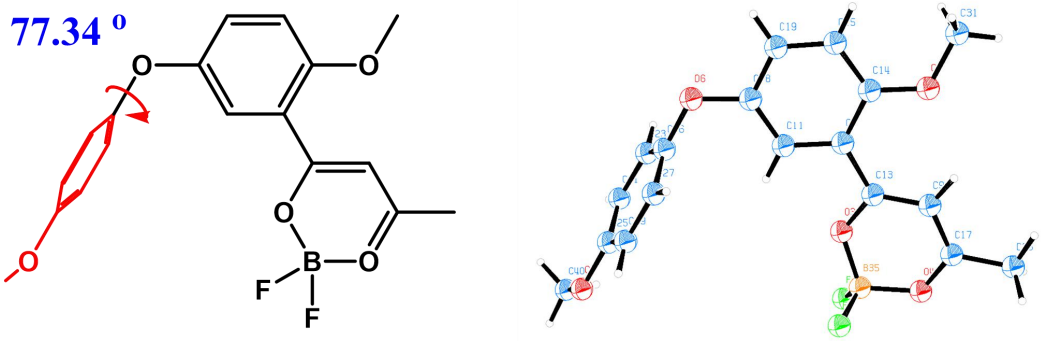

Figure S15. Chemdraw structure (left) and single crystal structure (right) of compound **5.**

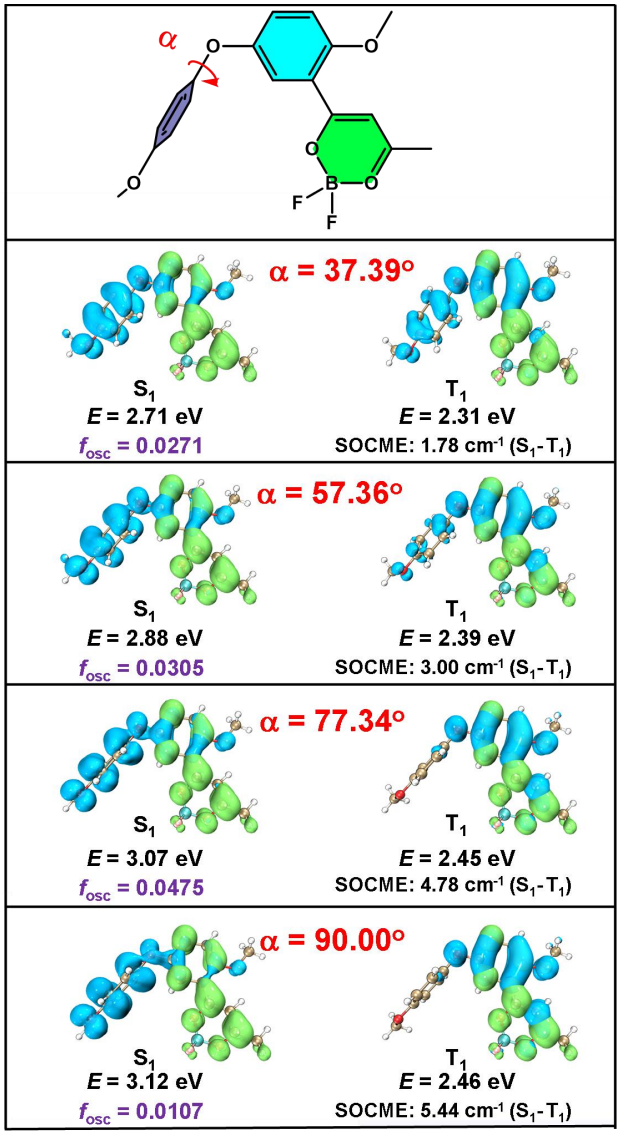

Figure S16. Dependence of excited state properties on the conformation of compound **5**; here the conformation is defined by the dihedral angle between the second anisole group and the dioxaborine plane.

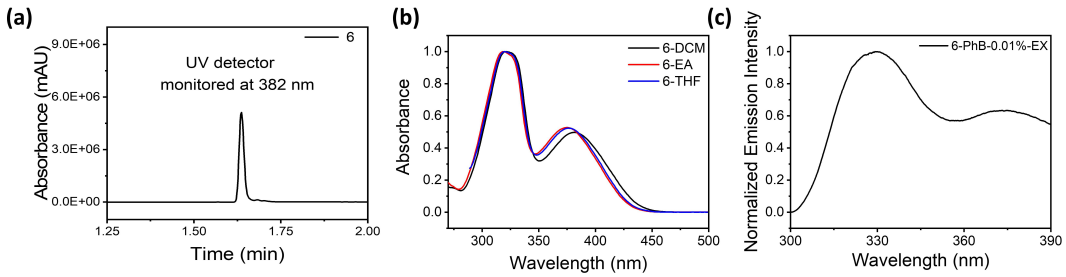

Figure S17. (a) HPLC profile of compound **6**. UV absorption was monitored at 382 nm. (b) UV-vis spectra of compound **6** in different solvents. DCM, EA and THF refer to dichloromethane, ethyl acetate and tetrahydrofuran, respectively. (c) Excitation spectra of **6**-PhB-0.01% samples. The high purity of **6** confirmed by HPLC measurement, as well as the similar maxima in UV-vis spectra and excitation spectra of **6**-PhB-0.01% melt casting materials, can rule out the contribution of impurity mechanism to the present afterglow material systems.

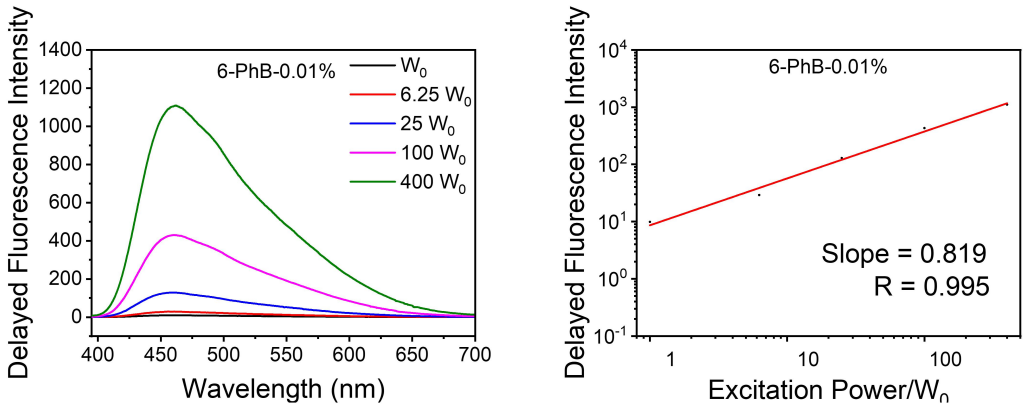

Figure S18. Power-dependent delayed fluorescence spectra of **6**-PhB-0.01% samples. It is found that the intensity of delayed fluorescence of the afterglow materials exhibit a quasi-linear dependence on the excitation dose, which further support the TADF mechanism.

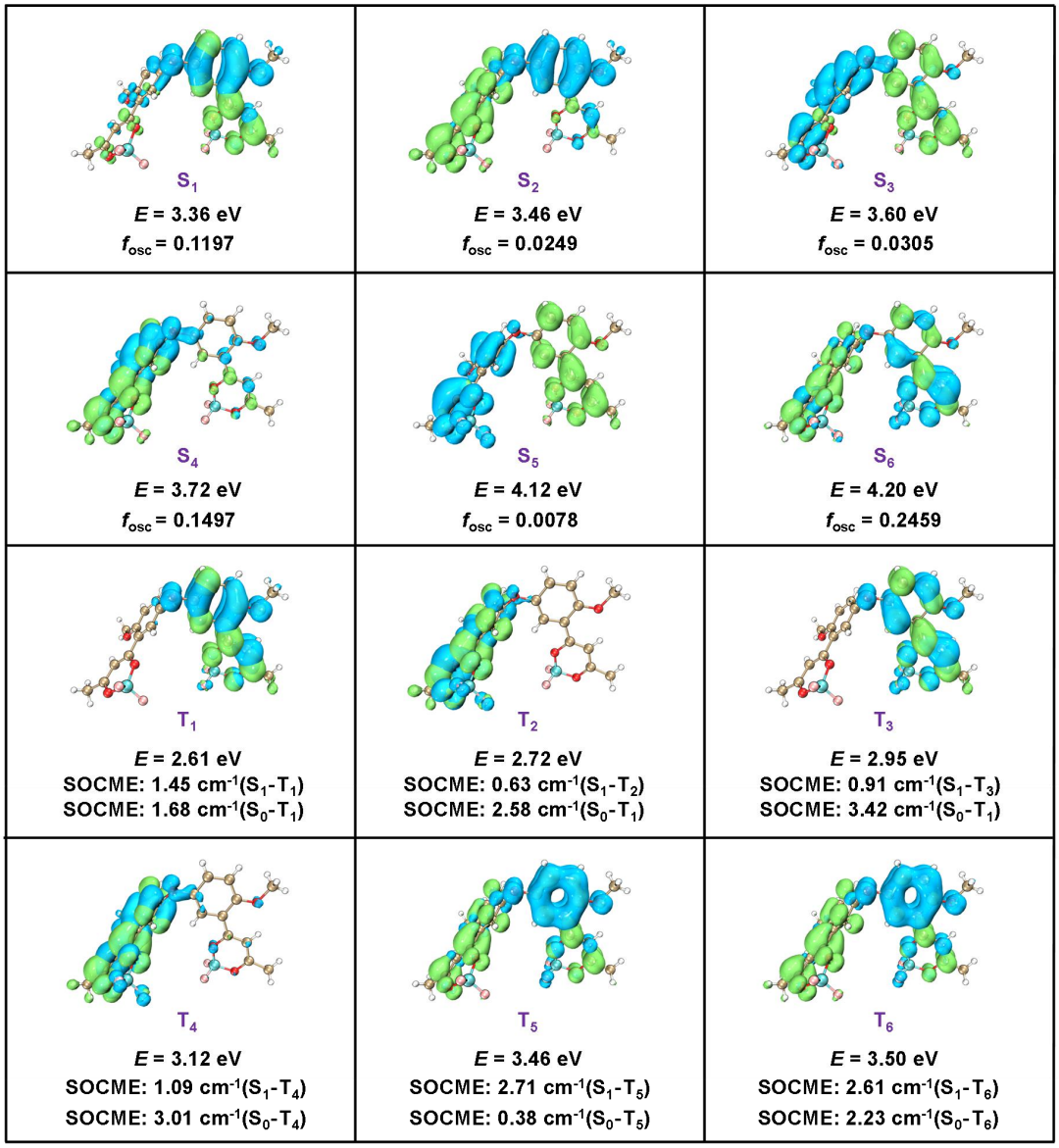

Figure S19. The TD-DFT calculated results of compound **6** singlet and triplet excited states. Despite that the singlet-triplet splitting energies ($\triangle E_{ST}$ = 0.43 eV) of **6**-PhB-0.01% system obtained from experimental results (S_1 level, 2.67 eV; T_1 level, 2.23 eV) are larger than those in **6**-PhB-0.01% system ($\triangle E_{ST}$ = 0.35 eV), there are rich S_1-to-T_n channels with SOCME values above 0.5 cm^{-1} and even 1.0 cm^{-1}. These would also enhance k_{RISC} of the **6**-PhB-0.01% to moderate values on the order of 10^0-10^1 s^{-1}, which agree well with the experimental observation (that is, the delayed fluorescence lifetimes 0.1 s to 1.0 s) of the **6**-PhB-0.01% materials under ambient conditions.

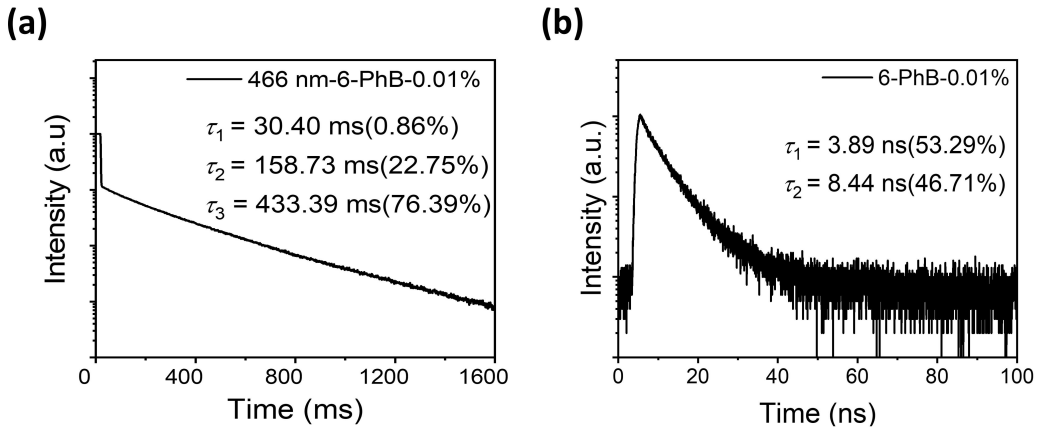

Figure S20. (a) Excited state decay profiles of **6**-PhB-0.01% melt-cast samples under ambient conditions. (b) The fluorescence decay profiles of **6**-PhB-0.01% melt-cast samples under ambient conditions.

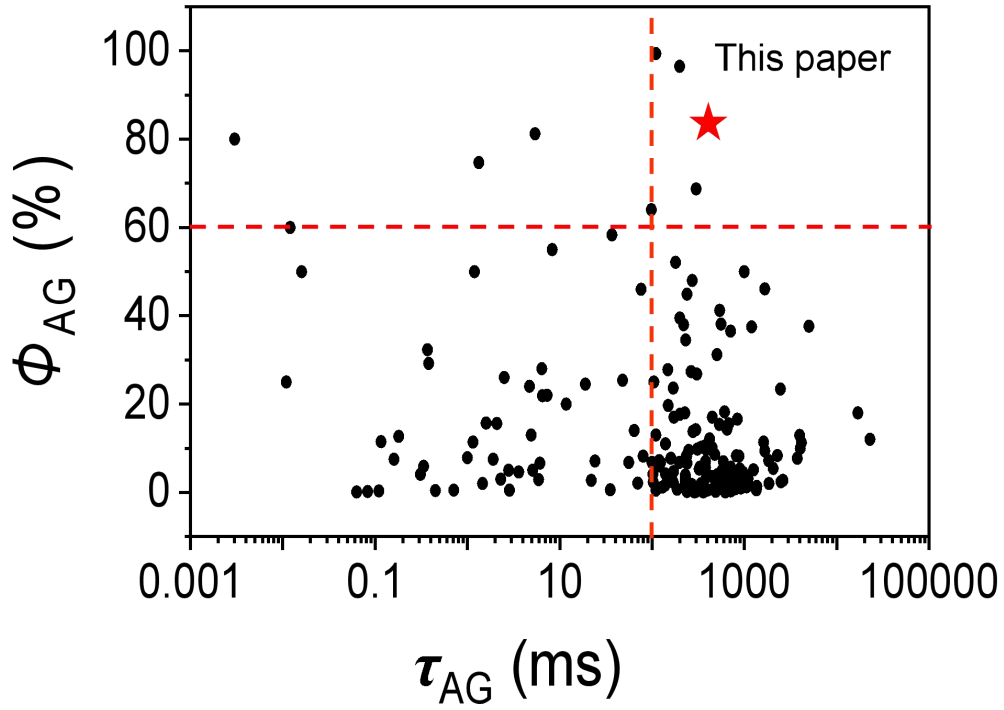

Figure S21. Afterglow quantum yields (Φ_{AG}) and afterglow emission lifetimes (τ_{AG}) of organic RTP and afterglow materials in the previously reported studies.

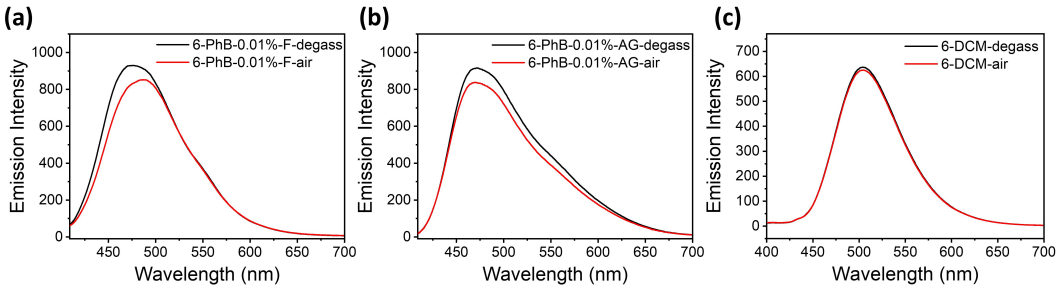

Figure S22. (a) Room-temperature steady-state emission spectra of **6**-PhB-0.01% melt-cast materials (black line, in degassed condition; red line, in aerated condition). (b) Delayed emission (1 ms delay) spectra of **6**-PhB-0.01% melt-cast materials (black line, in degassed condition; red line, in aerated condition). (c) Room-temperature steady-state emission spectra of compound **6** in dichloromethane (black line, in degassed condition; red line, in aerated condition).

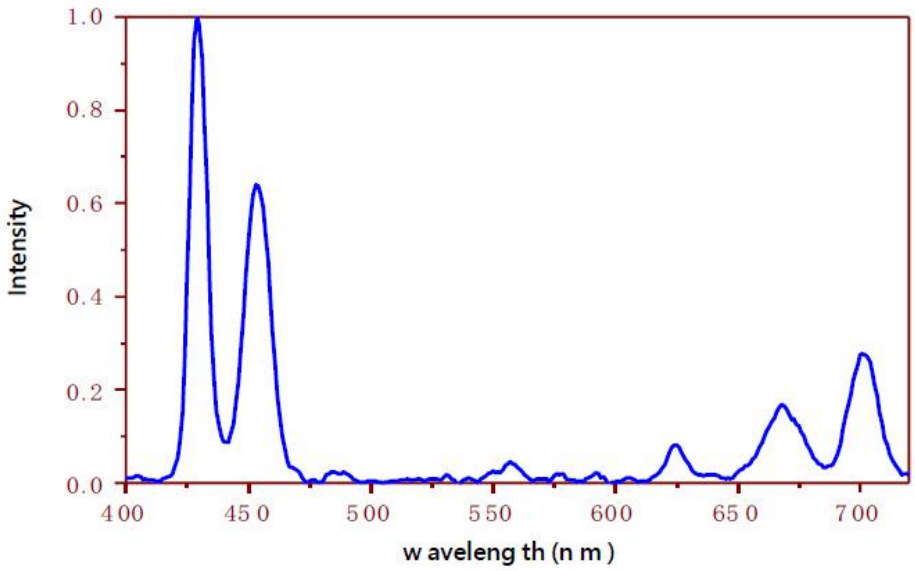

Figure S23. Emission spectra of blue up-conversion materials (excited at 980 nm) from the supplier. The blue up-conversion materials were purchased from Shenzhen Orient Color Change Technology Co Ltd. The blue up-conversion materials are crystalline powders with sizes of around 5 μm.

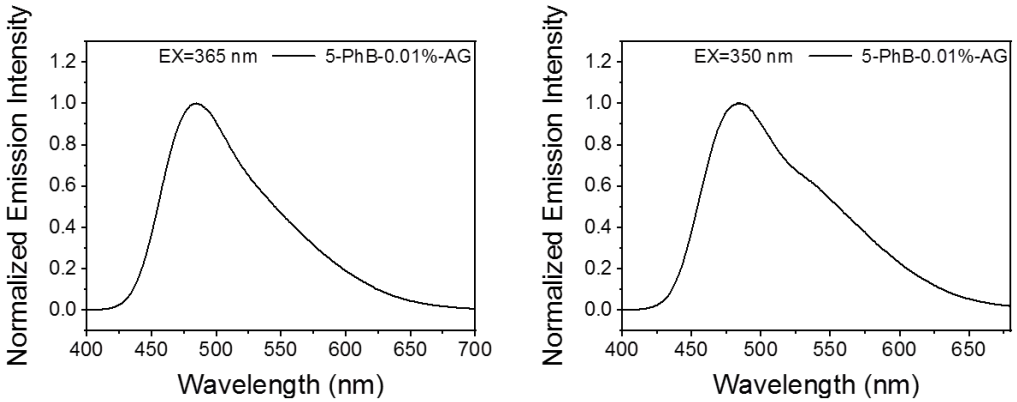

Figure S24. Delayed emission (1 ms delay) spectra of 5-PhB-0.01% materials excited at 365 nm and 350 nm.

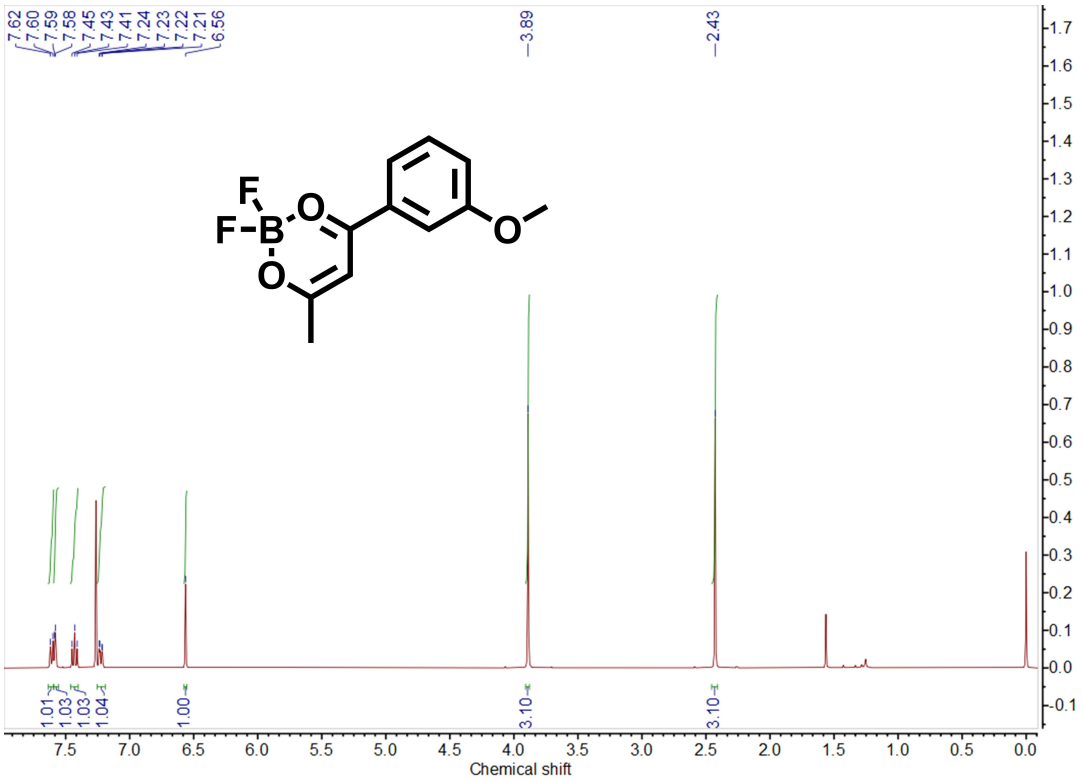

Figure S25. ^{1}H NMR spectra of compound **1**.

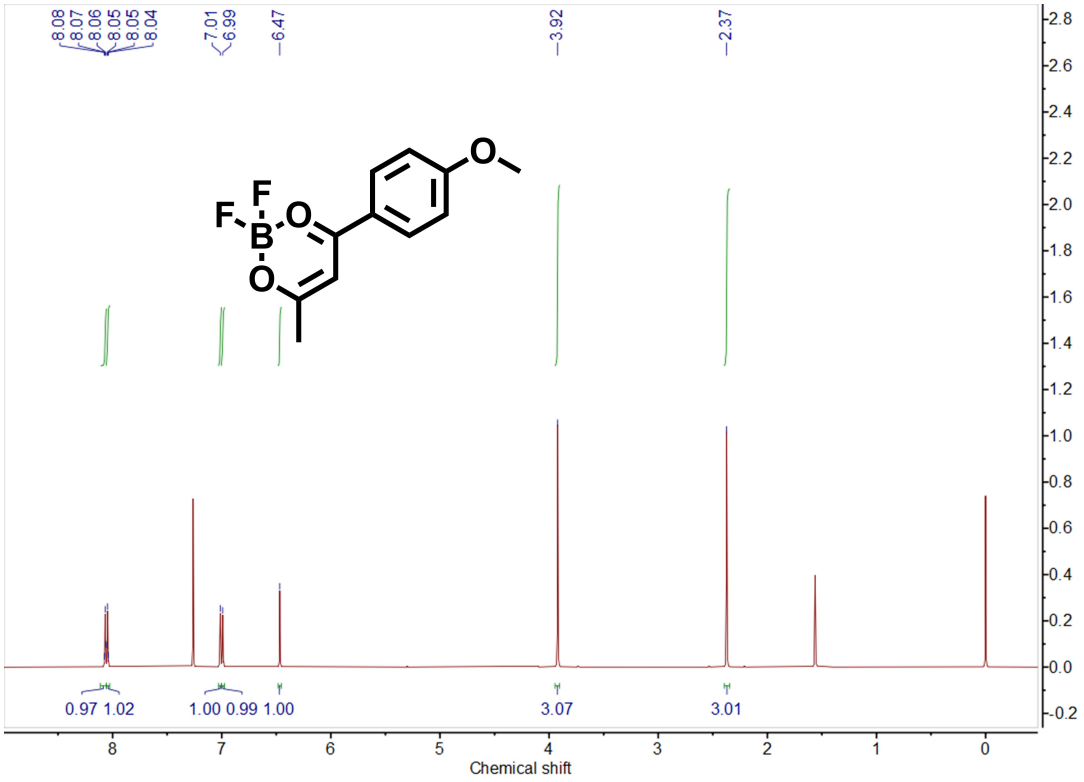

Figure S26. [1]H NMR spectra of compound **2**.

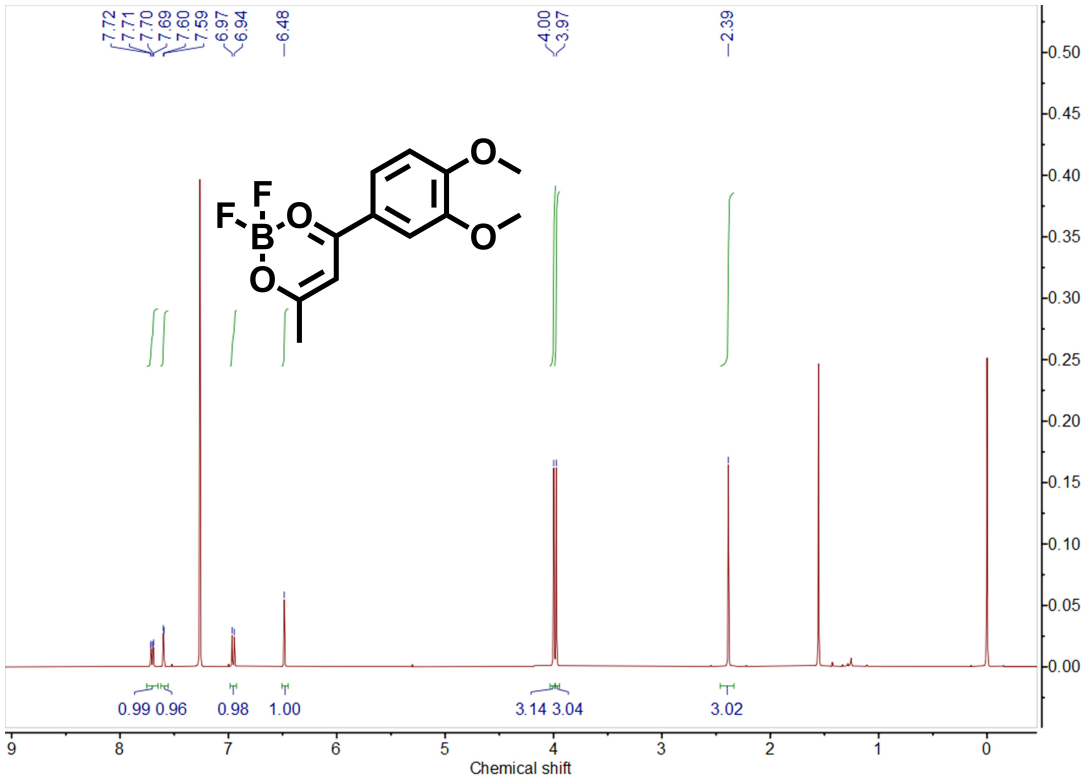

Figure S27. [1]H NMR spectra of compound **3**.

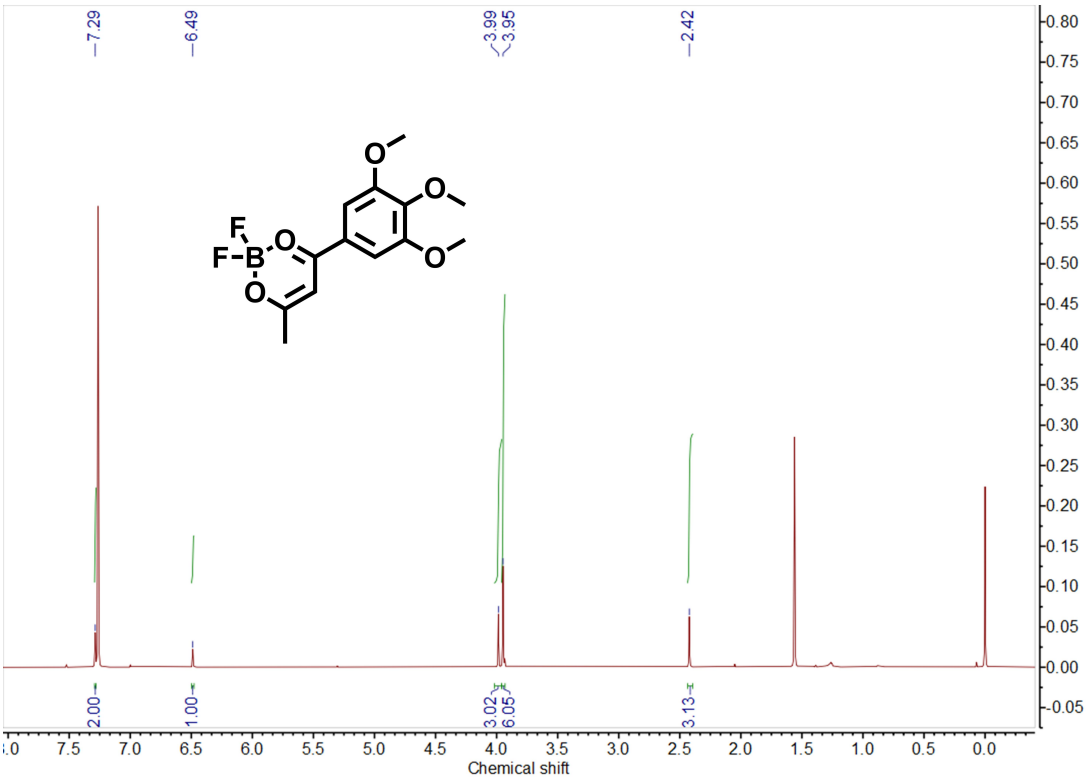

Figure S28. [1]H NMR spectra of compound **4**.

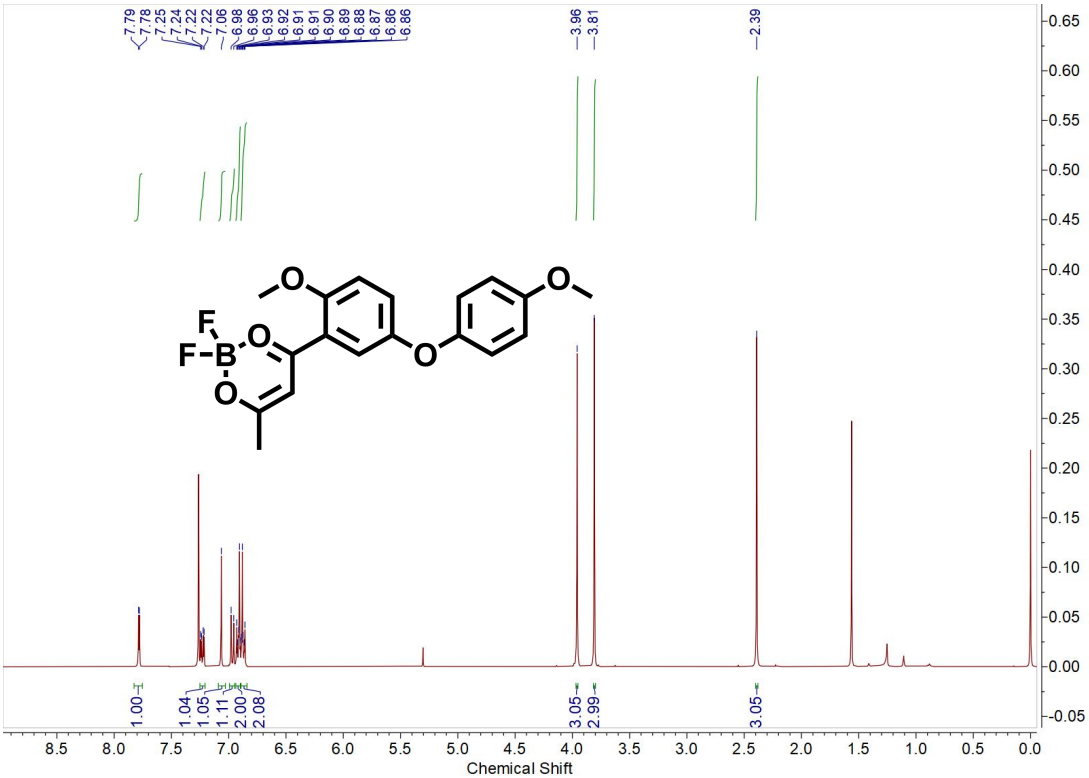

Figure S29. [1]H NMR spectra of compound **5**.

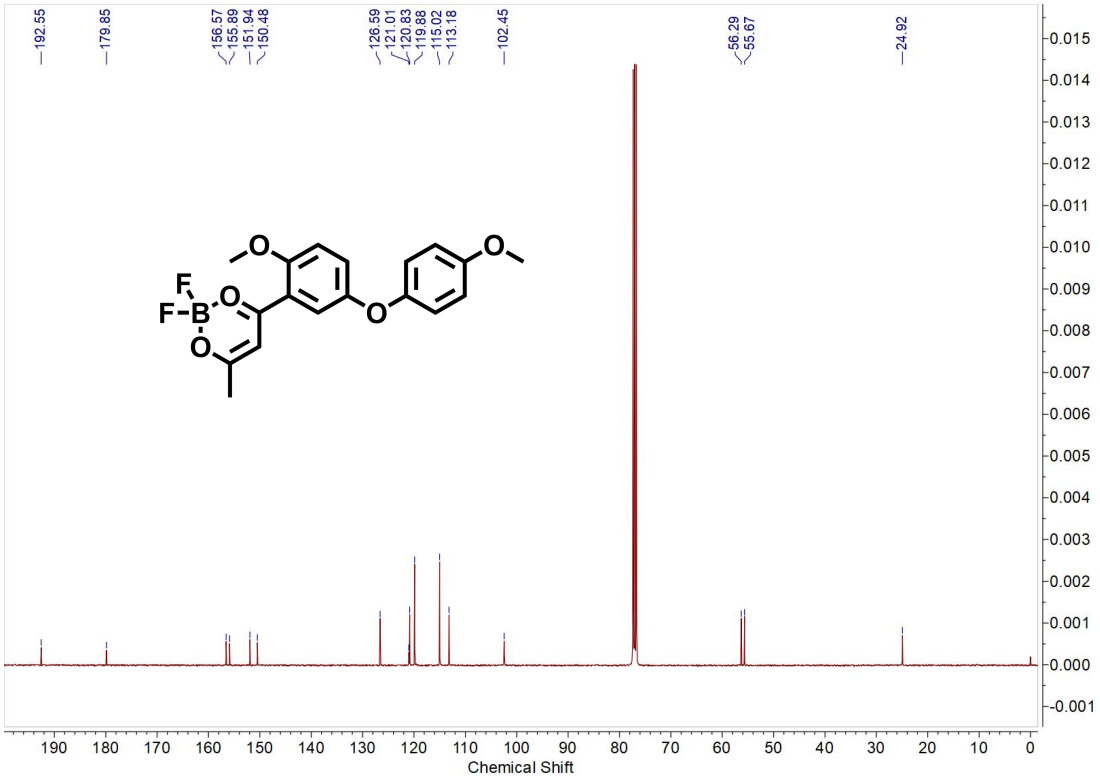

Figure S30. ^{13}C NMR spectra of compound **5**.

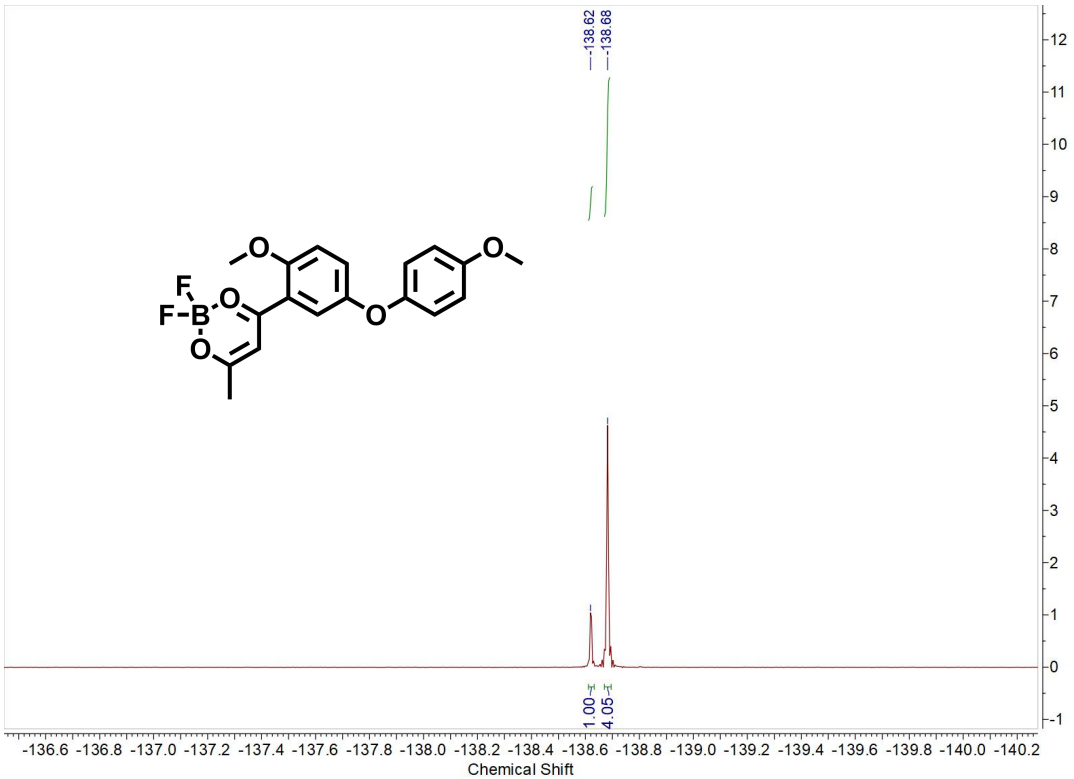

Figure S31. ^{19}F NMR spectra of compound **5**.

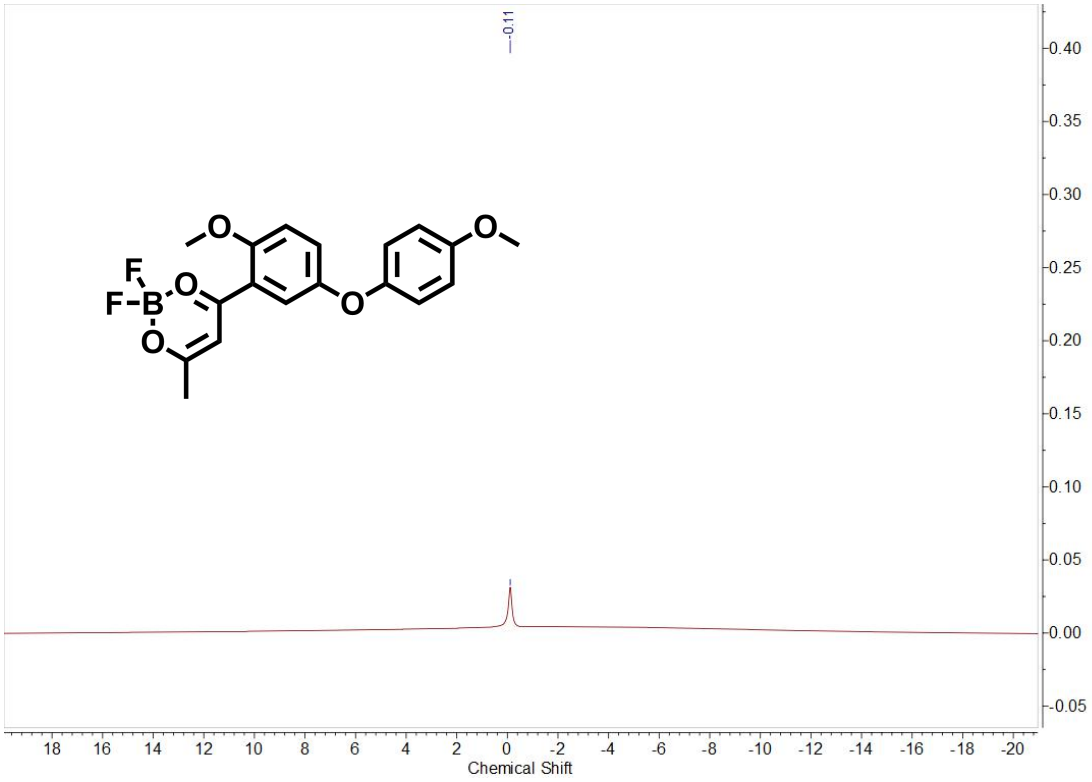

Figure S32. ^{11}B NMR spectra of compound **5**.

Qualitative Analysis Report

Data Filename	2019152-OMeEBM.d	**Sample Name**	OMeEBM
Sample Type	Sample	**Position**	Vial 49
Instrument Name	Instrument 1	**User Name**	
Acq Method	pub-LOWP-2_2.m	**Acquired Time**	2022/1/20 8:57:59 AM
IRM Calibration Status	Success	**DA Method**	PUB.m
Comment			

Sample Group	**Info.**
Acquisition SW Version	6200 series TOF/6500 series Q-TOF B.05.01 (B5125.3)

User Spectra

Fragmentor Voltage	Collision Energy	Ionization Mode
75	0	ESI

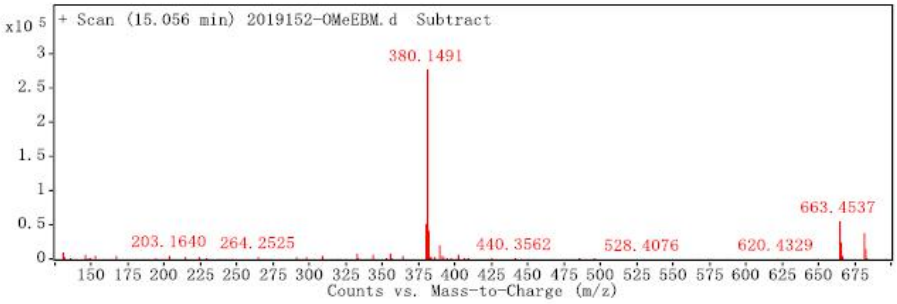

Peak List

m/z	z	Abund	Formula	Ion
379.1515	1	53177.3	C18 H17 B F2 O5	(M+NH4)+
380.1491	1	277995.47	C18 H17 B F2 O5	(M+NH4)+
381.1511	1	43863.39	C18 H17 B F2 O5	(M+NH4)+
382.1524	1	5294.01	C18 H17 B F2 O5	(M+NH4)+

Formula Calculator Element Limits

Element	Min	Max
C	3	60
H	0	120
O	1	10
B	1	3
F	1	5

Formula Calculator Results

Ion Formula	m/z	m/z (Calc)	DBE	Diff (ppm)	Score (MFG)
C15 H18 B3 F3 N O5	379.1515	379.1520	9	1.3	99.35
C15 H22 B F3 N O6	379.1515	379.1523	6	2.24	98.1
C18 H17 B3 F2 N O4	379.1515	379.1508	13	-1.86	98.69
C18 H21 B F2 N O5	379.1515	379.1512	10	-0.92	99.68

--- End Of Report ---

Figure S33. HRMS spectra of compound **5**.

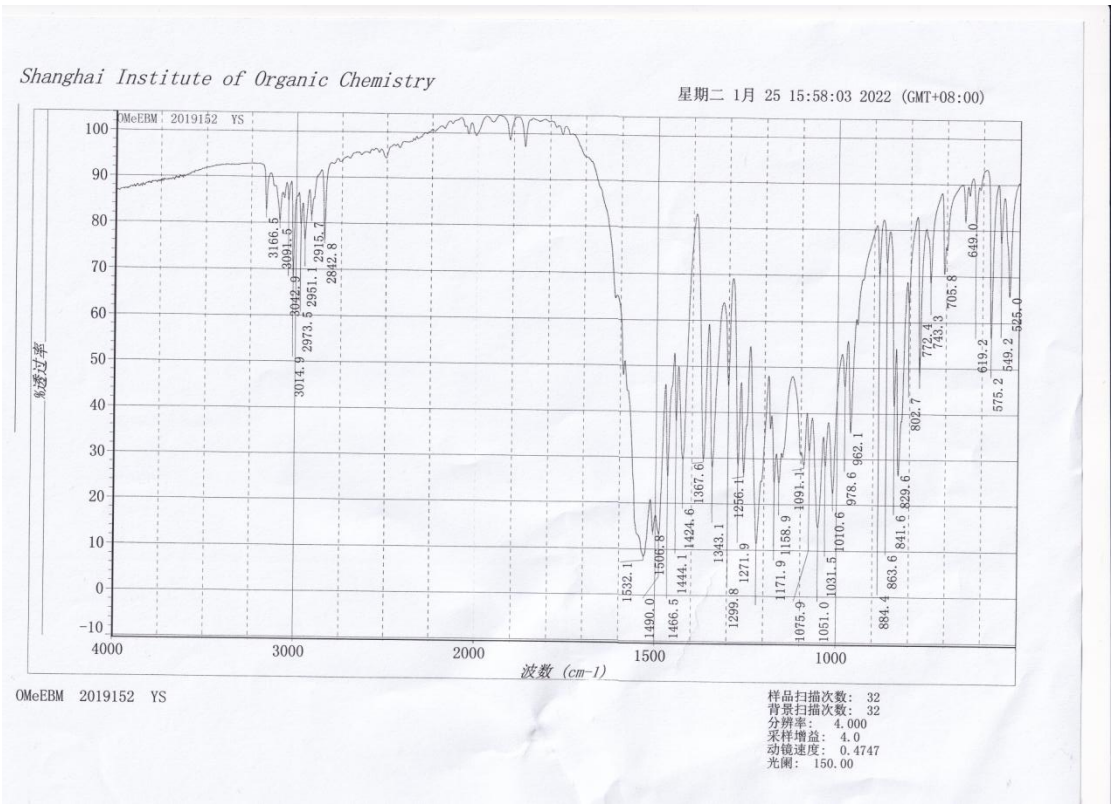

Figure 34. FT-IR spectra of compound **5**.

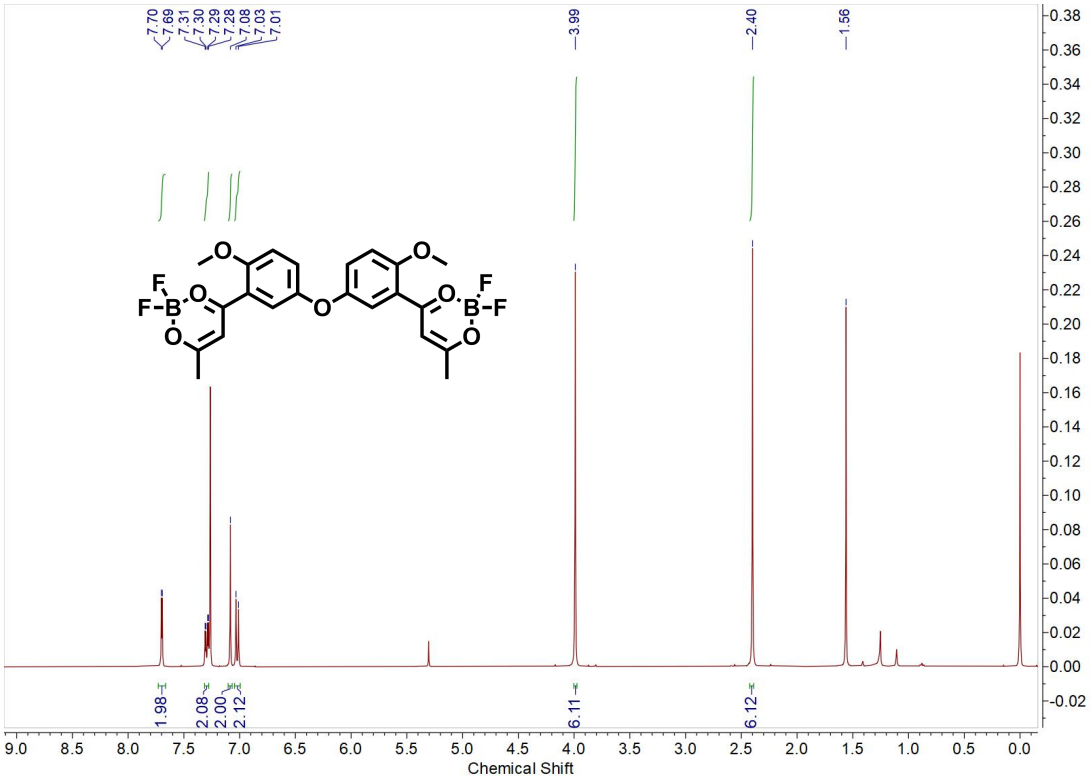

Figure S35. ^{1}H NMR spectra of compound **6**.

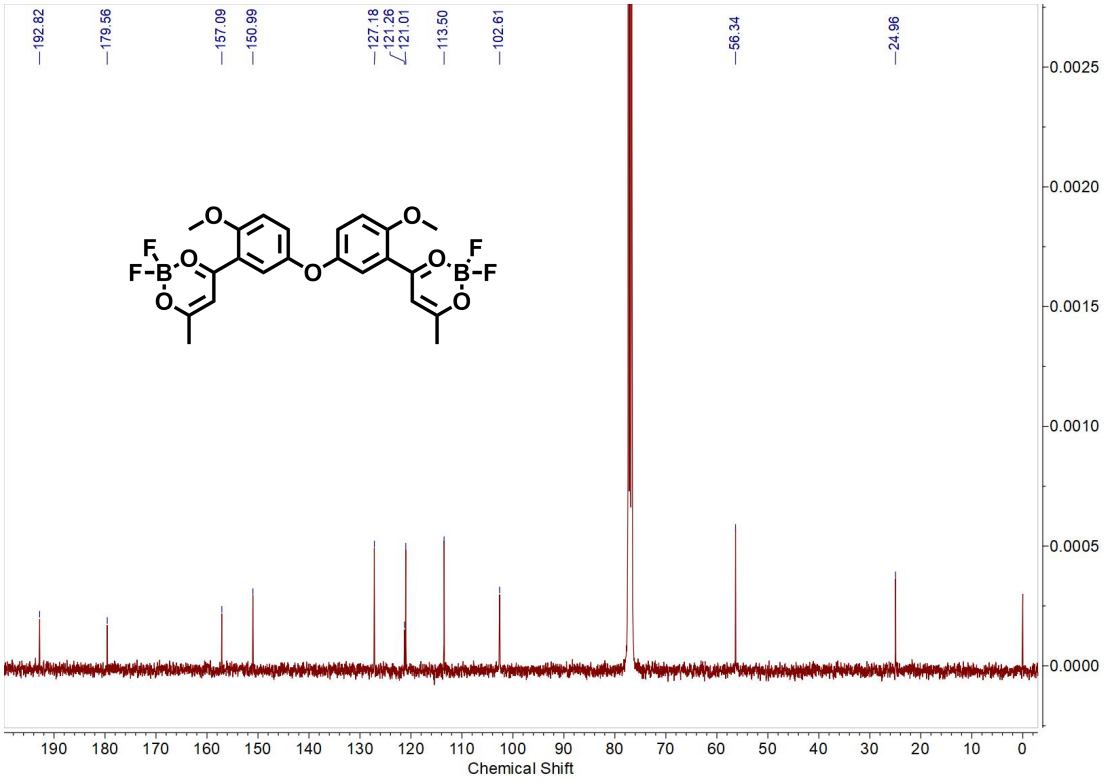

Figure S36. ^{13}C NMR spectra of compound **6**.

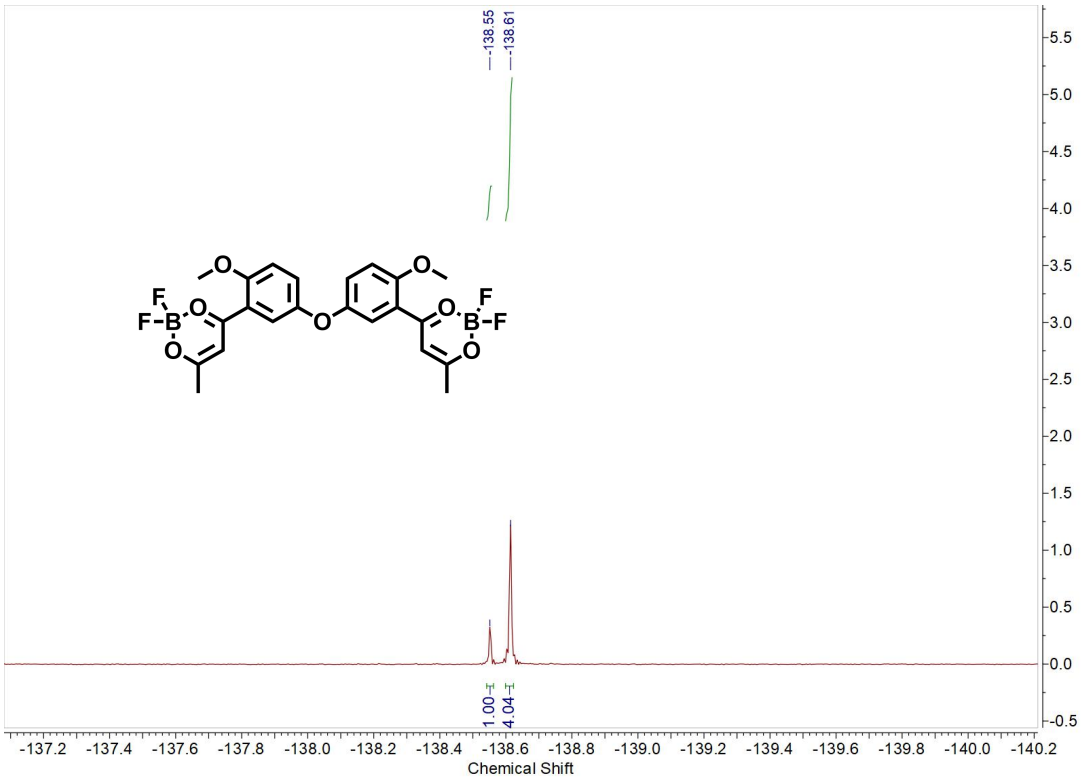

Figure S37. ^{19}F NMR spectra of compound **6**.

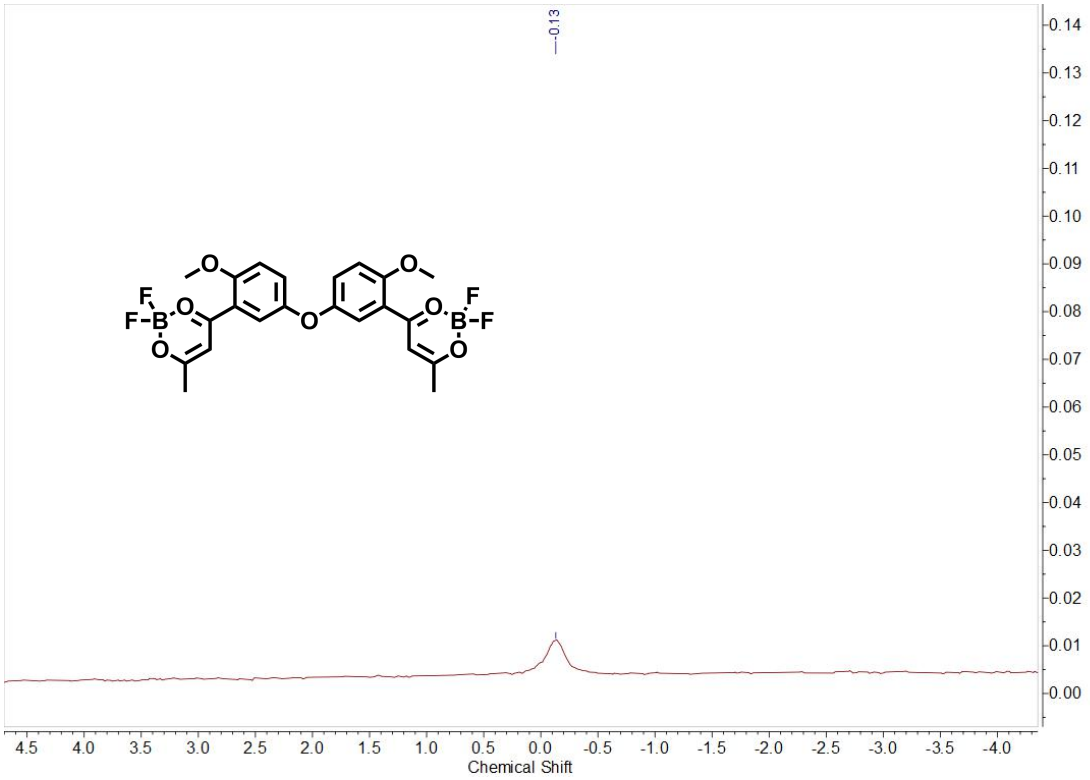

Figure S38. ^{11}B NMR spectra of compound **6**.

Qualitative Analysis Report

Data Filename	2019152-2OMeEBM.d	**Sample Name**	2OMeEBM
Sample Type	Sample	**Position**	Vial 50
Instrument Name	Instrument 1	**User Name**	
Acq Method	pub-LOWP-2_2.m	**Acquired Time**	2022/1/20 9:23:32 AM
IRM Calibration Status	Success	**DA Method**	PUB.m
Comment			

Sample Group	**Info.**
Acquisition SW Version	6200 series TOF/6500 series Q-TOF B.05.01 (B5125.3)

User Spectra

Fragmentor Voltage	Collision Energy	Ionization Mode
75	0	ESI

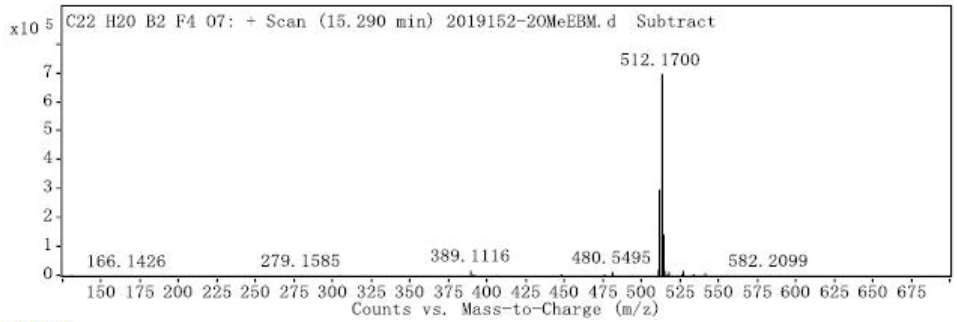

Peak List

m/z	z	Abund	Formula	Ion
510.1741	1	25446.1	C22 H20 B2 F4 O7	(M+NH4)+
511.1724	1	302982.19	C22 H20 B2 F4 O7	(M+NH4)+
512.1700	1	699214.75	C22 H20 B2 F4 O7	(M+NH4)+
513.1721	1	148375.69	C22 H20 B2 F4 O7	(M+NH4)+
514.1728	1	19802.9	C22 H20 B2 F4 O7	(M+NH4)+
515.1699	1	2306.97	C22 H20 B2 F4 O7	(M+NH4)+

Formula Calculator Element Limits

Element	Min	Max
C	3	60
H	0	120
O	1	10
B	1	3
F	2	6

Formula Calculator Results

Ion Formula	m/z	m/z (Calc)	DBE	Diff (ppm)	Score (MFG)
C19 H25 B2 F5 N O8	510.1741	510.1754	8	2.56	96.78
C22 H24 B2 F4 N O7	510.1741	510.1742	12	0.23	99.97
C25 H23 B2 F3 N O6	510.1741	510.1731	16	-2.09	97.83

--- End Of Report ---

Figure S39. HRMS spectra of compound **6**.

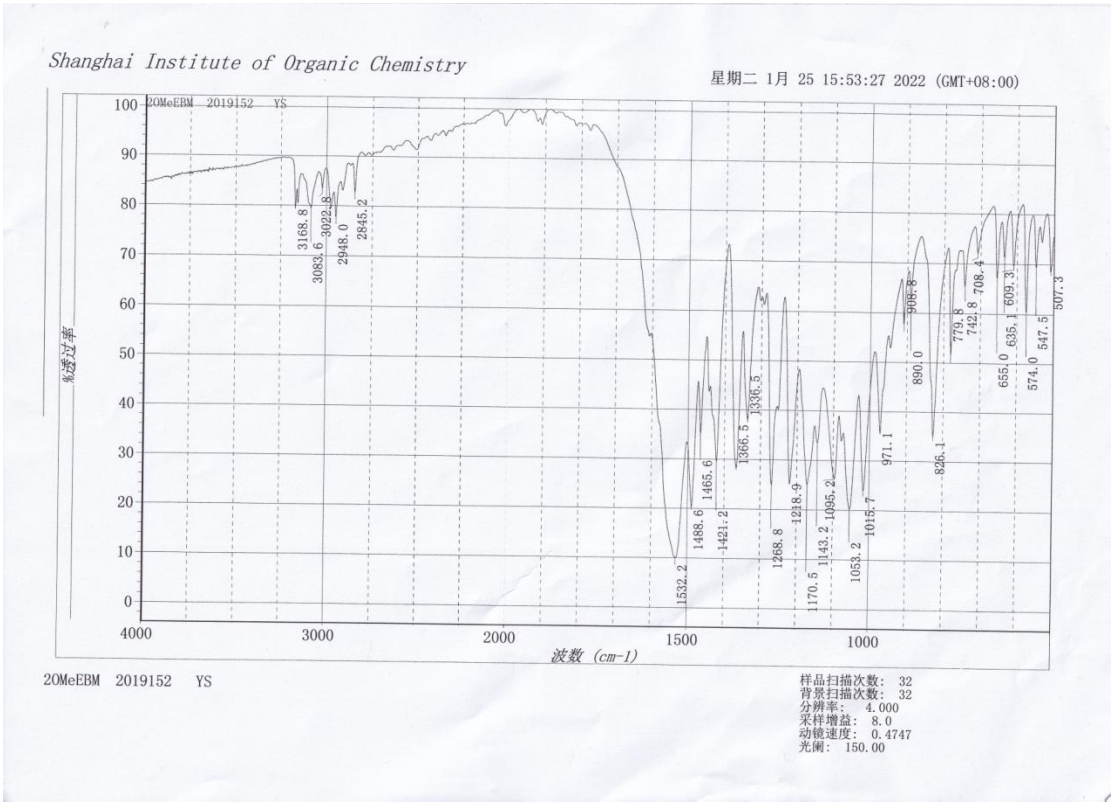

Figure S40. FT-IR spectra of compound **6**.